

Discovery of Reflection Nebulosity Around Five Vega-like Stars

Paul Kalas^{1,2}, James R. Graham^{1,2}, Steven Beckwith³,

David C. Jewitt⁴ and James P. Lloyd^{1,2}

`kalas@astron.berkeley.edu`

ABSTRACT

Coronagraphic optical observations of six Vega-like stars reveal reflection nebulosities, five of which were previously unknown. The nebulosities illuminated by HD 4881, HD 23362, HD 23680, HD 26676, and HD 49662 resemble that of the Pleiades, indicating an interstellar origin for dust grains. The reflection nebulosity around HD 123160 has a double-arm morphology, but no disk-like feature is seen as close as 2.5'' from the star in K-band adaptive optics data. We demonstrate that uniform density dust clouds surrounding HD 23362, HD 23680 and HD 123160 can account for the observed 12–100 μm spectral energy distributions. For HD 4881, HD 26676, and HD 49662 an additional emission source, such as from a circumstellar disk or non-equilibrium grain heating, is required to fit the 12–25 μm data. These results indicate that in some cases, particularly for Vega-like stars located beyond the Local Bubble (>100 pc), the dust responsible for excess thermal emission may originate from the interstellar medium rather than from a planetary debris system.

Subject headings: circumstellar matter—reflection nebulae— infrared: stars and ISM— instrumentation: adaptive optics

1. Introduction

The far-infrared (FIR), all-sky survey conducted by the Infrared Astronomical Satellite (IRAS) revealed that roughly 15% of nearby main sequence stars have excess thermal emission due to the presence of circumstellar dust (Backman & Gillett 1987; Aumann 1988; Plets 1999). The thermal

¹Astronomy Department, University of California, 601 Campbell Hall, Berkeley, CA 94720

²Center for Adaptive Optics, University of California, Santa Cruz, CA, 95064

³Space Telescope Science Institute, 3700 San Martin Drive, Baltimore, MD 21218

⁴University of Hawaii, 2680 Woodlawn Drive, Honolulu, HI 96822

excess was first discovered around Vega (Aumann et al. 1984), and approximately 100 main sequence stars display the “Vega Phenomenon” (Backman & Paresce 1993). The spectral energy distributions (SEDs) of Vega-like stars are typically fitted assuming disk-like distributions of grains (Sylvester & Skinner 1996), though in the optically thin regime the adopted geometry plays no role. Assuming the grains orbit the host stars as circumstellar disks, the dust destruction timescales are typically one or two orders of magnitude shorter than the stellar ages. The existence of unseen parent bodies, exosolar analogs to Kuiper Belt objects, is inferred in order to replenish the dust complex via collisional erosion (Backman & Paresce 1993).

High resolution imaging of Vega-like stars has confirmed the existence of circumstellar debris disks around ~ 7 main sequence stars (Kalas 1998; Lagrange et al. 2000). However, the ratio of debris disks inferred from the FIR SEDs, to those spatially resolved by imaging, is roughly 10:1. Here we present coronagraphic images of reflection nebulosity surrounding six main sequence stars previously identified as Vega-like (Backman & Paresce 1993; Sylvester et al. 1996). The new data show dust morphology that is not disk-like, but qualitatively resembles the Pleiades reflection nebulosity in five cases. Dust scattered light detected around HD 123160 shares characteristics with nebulosities seen in both the Pleiades and in star forming regions.

2. Observations & Data Reduction

We used an optical coronagraph at the University of Hawaii (UH) 2.2 m telescope to obtain CCD images in the *R*-band (Table 1). HD 123160 was also imaged in the *V*-band. Reimaging optics gave $0.4''$ per pixel, sufficient to Nyquist sample the $\sim 1.2''$ full-width at half-maximum (FWHM) point-spread function (PSF). The field of view was a circular region with diameter $5.5'$.

Follow-up observations were obtained in the near-infrared (NIR) for HD 123160 using the Lick Observatory 3 m telescope (Table 1). A 256×256 pixel ($0.076''/\text{pixel}$), coronagraphic, near-infrared camera was used to artificially eclipse the central star with a $0.7''$ wide finger (Lloyd et al. 2000). Adaptive optics compensation (Max et al. 1997) using the primary star as a wavefront reference source improved image quality from $\sim 1''$ intrinsic seeing to $\sim 0.16''$ (FWHM).

Our target sample was compiled from lists of Vega-like stars published by Sylvester et al. (1996) and Backman & Paresce (1993). We imaged all 22 Vega-like stars from Table 16 in Sylvester et al. (1996), and 38 of the 60 stars from Table VIII in Backman & Paresce (1993). The total sample of 79 stars (the two tables have three stars in common) includes several with resolved debris disks (β Pic, Vega, ϵ Eri, and Fomalhaut), two members of the Pleiades (18 Tau and 21 Tau), and three Herbig Ae/Be stars (HD 34282, HD 35187, and HD 141569). We also observed stars nearby in the sky and with magnitudes comparable to the science targets to be used later as template stars for PSF subtraction.

Data reduction followed the standard steps of bias subtraction, flat-fielding, sky subtraction, image registration, and median-filtering of multiple frames to attain the effective integration times

listed in Table 1. The PSF of each science target was subtracted by using either template PSFs discussed above, or by radially sampling the template PSF, fitting the data with a 7th order polynomial, and producing an artificial PSF from this fit. The PSF subtraction step is useful for extracting faint nebulosity as close to the star as possible, but the nebulosities discussed here are detected in raw data. Residual noise after the PSF subtraction dominates the data $\sim 1''$ beyond the edge of the occulting spot. Table 1 lists the radius centered on each target star below which we cannot obtain reliable information about the circumstellar environment.

3. Results

The suppression of direct stellar light with the coronagraph reveals the presence of faint reflection nebulosity around the six Vega-like stars in Table 1 and Fig. 1. The nebulosites have the following general properties: (a) spatial extent $\sim 1' - 2'$ radius; (b) surface brightness varying as radius, $r^{-\beta}$, with $\beta \leq 2$; (c) range of surface brightness approximately 20 mag arcsec^{-2} to 24 mag arcsec^{-2} ; and (d) linear, filamentary, striated morphological structure, similar to that observed in the Pleiades reflection nebulosities (Arny 1977). The background noise, $3\sigma \sim 24$ mag arcsec^{-2} , limits the radial extent to which each nebulosity is detected. Table 1 gives the *Hipparcos* parallaxes, indicating heliocentric distances > 100 pc for every star. The detected nebulosities therefore span spatial scales $10^3 - 10^5$ AU from their parent stars, and the occulted regions obscure the central $\sim 10^3$ AU (Table 1).

The nebulosity around HD 26676 (Fig. 1D), the brightest and most extended, has been previously documented by van den Bergh (1966) and identified as a member of the Tau R2 association (Racine 1968), which is part of the Pleiades. An examination of the literature indicates that the other five nebulosities were not previously known.

The nebulosity around HD 123160 is characterized by a double-arm structure southeast of the star (Fig. 1F; Features *i* and *ii*), rather than the linear features seen around the other five stars. Arm-like morphologies appear near several pre-main sequence stars such as GM Aur and Z CMa (Nakajima & Golimowski 1995). The outside boundary of arm *i* traces a closed curve that intersects feature *iii*. The latter is curved in the same direction as *i*, indicating that *iii* may be a detached segment of *i*. Another diffuse, curved structure, *iv*, is $95''$ from the star with position angle and curved morphology comparable to feature *iii*. Neither *iii* nor *iv* have a core+halo structure that characterizes background field galaxies in these data. We also detect two point sources lying along a north-south axis and separated by $3.6''$ at position *v*. They are surrounded by a nebulosity that has a tail pointing towards HD 123160. Both are red, with $V - K = 1.7$ mag and 1.1 mag for the north and south stars, respectively (after applying the extinction correction determined for HD 123160 in Table 3). The colors of the northern component are consistent with a late-type stellar photosphere. However, the southern component has $H - K = 1.1$ mag, indicating an additional source of near-infrared emission such as from a circumstellar disk (Meyer, Calvet & Hillenbrand 1997).

Figure 2 shows that two brightness knots exist within arm *ii*. In the K-band adaptive optics data, the north knot, *ii*a, contains a point-like source $9.7 \pm 0.2''$ from the star superimposed on the broader nebular emission. After subtracting an estimate for the background contributed by the broader nebulosity, the point-like source has $V=16.5 \pm 0.3$ mag and $K=14.2 \pm 0.3$ mag (extinction corrected; Table 3). The $V - K$ color is consistent with a K dwarf spectral type and distance modulus > 100 pc. Compared to the optical data, the adaptive optics *K*-band data probe closer to the star for any structure that may have a disk-like morphology. No circumstellar disk is detected as close as $\sim 2.5''$ from the primary.

Aperture photometry (diameter = $4.0''$) performed on the nebulosities labeled in Figs. 1F and 2 gives *R* and *V*-band fluxes that decrease radially from the star with $\beta \leq 1$, rather than $\beta = 2$ or $\beta = 3$ that would characterize a homogenous medium or dust disk, respectively. For example, *iii* has 9% the flux of *ii*a, but is 5 times farther from the primary. If both features are produced by grains with similar scattering properties, then *iii* has approximately twice as many scattering grains as *ii*a. The $V - R$ colors range from 0.0 to -0.2 mag after an extinction correction is applied. Using $R=7.81$ mag for HD 123160 (Sylvester et al. 1996), $V - R = +0.2$ mag if HD 123160 is a G5V star, or $V - R = +0.3$ mag if it is a G0III star. Therefore the nebulous features in Figs. 1F and 2 appear bluer than HD 123160, consistent with the scattered-light colors of the Merope nebula (Herbig 1996; Herbig & Simon 2001).

The discovery of nebulosity around these Vega-like stars that is not disk-like raises the question of whether or not the dust emitting in the FIR is contained in disks related to planet building, or merely due to dust contained in the ISM. The “Pleiades Phenomenon” is due to the chance encounter of bright, nearby stars with a clump of ISM (Arny 1977; White & Bally 1993; Herbig & Simon 2001). Filamentary features in optical scattered light are produced by the shearing of the cloud as radiation pressure pushes dust around each star. Our data do not necessarily exclude the existence of circumstellar disks in addition to the Pleiades-like nebulosity because the observations are not sensitive to the central $\sim 4''$ radius (Table 1). However, the main reason to presume the existence of a circumstellar disk is that the IRAS data give fluxes in excess of photospheric levels. If the Pleiades-like dust detected here is capable of producing the FIR emission, then the Pleiades Phenomenon is a more plausible explanation for the FIR excesses than the Vega Phenomenon. Below we test the validity of attributing the observed excess FIR emission to an interstellar dust cloud encountering each of our target stars.

4. Thermal Emission Model for the Pleiades Phenomenon

To test if the IRAS far-infrared data are consistent with the Pleiades Phenomenon, we experiment with a model comprising a star embedded in a uniform number density, optically thin, dust cloud. The geometry is spherical, except that radiation pressure from the star excavates an axisymmetric paraboloidal cavity within the cloud, as described by Artymowicz & Clampin (1997). In spherical coordinates, (r, θ, ϕ) , a volume element is given as $dV = dr \times r \sin\theta d\phi \times r d\theta$. The

inner boundary of the cloud cavity has radius,

$$r = r_{in} \left(\frac{2}{1 + \cos\theta} \right) \quad (1)$$

The smallest radius that grains can approach the star, r_{in} , depends on the relative velocity and the force of radiation pressure (which scales with stellar luminosity and grain properties, such as size). For example, at a relative velocity of 12.2 km s^{-1} , grains $<0.2 \mu\text{m}$ in size will not approach Vega closer than $\sim 2000 \text{ AU}$, whereas $1 \mu\text{m}$ sized grains will reach as close as $\sim 200 \text{ AU}$ (Artymowicz & Clampin 1997). In our simulations r_{in} is a free parameter.

Grain temperatures are calculated in each volume element assuming grains receive blackbody radiation from the star, and emit as blackbodies. Grain absorption and emission efficiencies will depend on grain properties and wavelength regimes. We estimate the absorption and emission efficiencies empirically by assuming that they have the same functional form as the extinction function for interstellar grains given by Mathis (1990) in his Table 1. A smoothed version of this extinction function can be described by three power laws with form $\epsilon(\nu) = \epsilon_0 \nu^\alpha$, where $\alpha=0$ for $\lambda < 0.5 \mu\text{m}$, $\alpha=1.68$ for $0.5 \mu\text{m} \leq \lambda < 5 \mu\text{m}$, and $\alpha=1.06$ for $\lambda \geq 5 \mu\text{m}$. Very hot stars will put out their energy at short wavelengths where the grain absorption efficiency is at a maximum, whereas cool stars will not efficiently heat these interstellar grains. Most of the energy re-radiated by grains will occur in the $\lambda \geq 5 \mu\text{m}$ regime, and therefore will have emission efficiency proportional to $\nu^{1.06}$.

The dust cloud thermal emission is fitted to the observed IRAS fluxes by adjusting the grain number density, ρ , the inner minimum radius of the cavity, r_{in} , and the outer radius of the cloud, R_{out} . The photospheric contribution from optical wavelengths through $12 \mu\text{m}$ is fit by adjusting the stellar temperature, radius, and heliocentric distance. In the first iteration the stellar temperature and radius are taken from Cox (1999) based on the spectral type for each star given in the literature.

Table 2 gives the observed optical, near-infrared, and far-infrared magnitudes and fluxes. Interstellar reddening and extinction were calculated using both the B–V and V–K colors and is given in Table 3; we used $R_V=3.1$ for the total-to-selective extinction values given by Mathis (1990) in his Table 1. The color correction for the FIR data was obtained from Table VI.C.6 in the *IRAS Explanatory Supplement Version 2*. In Table 4 we list the extinction-corrected optical and NIR photometry, and the IRAS fluxes color-corrected based on the temperatures listed in Table 1. In several cases an alternate spectral type is proposed and the extinction and photometry are recalculated. We considered both the IRAS PSC and the FSC data for fitting the model to the $12\text{--}100 \mu\text{m}$ fluxes. The uncertainties for these data are given in the respective IRAS catalogs, with typical values $\sim 10\%$. The heliocentric distances used in the first iteration are taken from the *Hipparcos* parallaxes for each star (Table 1), but beyond 100 pc the *Hipparcos* distances have significant uncertainties.

Table 5 gives two examples of model fits to the SED of each star, and Figs. 3 - 10 display

the model fits as discussed below. Table 5 also lists the maximum grain temperature, T_o , the fractional infrared luminosity of the cloud, L_d/L_\star and the maximum optical depth, τ_{max} . For HD 4881, HD 26676 and HD 49662, the model fits to the 60–100 μm emission gives a deficit of 12–25 μm emission. Our simple model assumptions do not account for at least four factors that could enhance the 12–25 μm emission.

First, density variations exist within the dust cloud, as shown in the optical images (Fig. 1). The theoretical model of Artymowicz & Clampin (1997) also shows that a “snowplow” effect occurs as the dust moves around the cavity maintained by radiation pressure. A skin of higher density material will exist near the surface of the cavity. If we assume that the cavity is a sphere for simplicity, and displace the material that would have occupied the sphere to an annular skin with thickness $\Delta r = r_s - r_{in}$, then the mass density in the skin is:

$$\frac{\rho_{skin}}{\rho_{cloud}} = 1 + \left(\frac{r_{in}^3}{r_s^3 - r_{in}^3} \right) \quad (2)$$

The larger the dust cavity produced by the star, the denser the skin layer for a fixed skin thickness. For example, ρ is a factor of two greater in the skin compared to the ambient cloud for $r_{in}=200$ AU and $r_s=250$ AU, and a factor of 3 greater if we assume $r_{in}=500$ AU and $r_s=550$ AU. We find that including a high density surface layer in the model increases the 12–25 μm emission slightly, but a good fit to the data requires a factor of $\sim 10^2$ increase in dust density between the skin and the ambient material. Thus, the enhanced 12–25 μm emission must have additional sources.

Second, larger grains ($\geq 1 \mu\text{m}$) will not be pushed back by radiation pressure and will occupy the cavity (Artymowicz & Clampin 1997). We find that filling the cavity with grains also does not succeed in fitting the observed 12–25 μm emission, given no increase in the density of material above the ambient medium (Table 5).

Third, the smallest grains ($\leq 0.1 \mu\text{m}$) will undergo non-thermal heating events to ~ 1000 K (Greenberg 1968; Sellgren 1984). The empirical finding for the Pleiades is that the 12–25 μm emission should represent $\sim 30\%$ of the total nebular FIR flux (Castelaz et al. 1987; Sellgren et al. 1990). The IRAS SED’s for four stars in the Pleiades show that the 12–25 μm flux densities lie significantly above a blackbody fitting the 60–100 μm data (Castelaz et al. 1987). Thus, a hot grain component could be present that will add 12–25 μm flux that is not accounted for by our model. However, the existence of small-grain heating should also produce observable NIR excess emission and infrared emission features (Desert et al. 1990; Sellgren et al. 1996; Sylvester et al. 1997).

Fourth, our simulation does not take into account the existence of a circumstellar disk in addition to the ISM nebulosity detected in this paper. Material close to the star with number density decreasing with radius would add 12–25 μm flux to our model SED. Future high resolution observations are required to detect number density variations closer to the star than our observations

permit (Table 1). In four cases below we discuss previous attempts to fit the SED’s with model circumstellar disks.

4.1. 18 Tau and 21 Tau

Before applying our model to the stars shown in Fig. 1, we test it on two Pleiads that are in the IRAS PSC and FSC, and have been identified as candidate Vega-like stars (Backman & Paresce 1993). 18 Tau (HD 23324) and 21 Tau (HD 23432) are both B8V stars with *Hipparcos* distances between 110 pc and 120 pc. Two model fits to the SED of each star are given in Figs. 3 and 4, and Table 5. The parameters for models 18 Tau-a are chosen to produce a SED that fits the PSC 100 μm data. Model 18 Tau-b demonstrates that a fit to the FSC 100 μm point requires decreasing the mass density, ρ , and increasing the outer radius, R_{out} , relative to model 18 Tau-a. However, no combination of parameters can fit the 12–25 μm and the 60–100 μm regions simultaneously, in agreement with the findings of Castelaz et al. (1987). These authors suggest that the non-equilibrium heating of small grains may account for the observed excess flux in the IRAS 12 and 25 μm passbands. The angular radii of models 18 Tau-a and 18 Tau-b would be 8' and 21', respectively. Gaustad & Van Buren (1993) measure 8' radius for 18 Tau in the IRAS Infrared Sky Survey Atlas (ISSA). Thus, model 18 Tau-a is preferred over 18 Tau-b.

For a straightforward comparison, the model fits to the 21 Tau data use the same stellar parameters as the 18 Tau models. Model 21 Tau-a fits the IRAS 60–100 μm PSC data and again demonstrates that a second source of 12–25 μm emission is necessary. Relative to the 18 Tau models, we decrease the inner radius to 10 AU to show that the hotter grains do not add enough 12–25 μm flux to match the observations. However, the 60 μm flux density for 21 Tau in the IRAS FSC is significantly higher than in the PSC. Model 21 Tau-b gives a fit to the FSC data that agrees with the entire observed 12–100 μm SED. Thus, the errors in any single FIR data point may change the physical interpretation significantly. The angular radii of models 21 Tau-a and 21 Tau-b would be 8' and 3.7', respectively. Gaustad & Van Buren (1993) measure 5' radius for 21 Tau in ISSA maps. Thus, model 21 Tau-b is preferred over 18 Tau-a.

4.2. HD 4881

Given the B9.5V spectral type for HD 4881, our model gives optical-NIR flux densities that lie well below the observed values if we assume the *Hipparcos* distance of 350 pc (Table 1) and $T_{eff}=11,400$ K. Rather, the fit to the optical and NIR data shown in Fig. 5 assumes $d=168$ pc and $T_{eff}=12,300$ K. The higher temperature is consistent with the Miroshnichenko et al. (1999) reclassification of this star as B8. The 25–100 μm fluxes are fitted with the dust cloud parameters given in Table 5. Figure 5 maps the spectral energy distributions of two model fits. Fitting the 100 μm photometry requires that R_{out} is not smaller than $\sim 8.7 \times 10^4$ AU. At the assumed distance,

the model dust cloud subtends $\sim 8.6'$ radius, which is approximately equal to the average angular extent measured by Dring et al. (1996) in IRAS Skyflux plates. This is larger than the $\sim 5'$ radial extent measured by Gaustad & Van Buren (1993) and Miroshnichenko et al. (1999), but a factor of two uncertainty in the measured angular extent has been demonstrated by Jura (1999). We find that r_{in} may be varied between 1 AU and 800 AU with the resulting 25 μm flux density contained within the IRAS PSC and FSC data points, and with negligible effect on the 12 μm flux density.

At 12 μm our model photosphere+cloud gives $F_{12}=0.13$ Jy, whereas the observed IRAS values are 0.19 ± 0.02 Jy in the PSC, and 0.25 ± 0.02 Jy in the FSC. A poor fit to the 12 μm flux was previously found in circumstellar disk models for HD 4881 (Coulson et al. 1998), as well as models that assume spherical dust clouds (Miroshnichenko et al. 1999). Here the 0.06 Jy difference between the flux density in our model and the PSC flux density is equal to the disagreement between the PSC and FSC flux densities. The statistical significance of the poor model fit is therefore best evaluated after follow-up 10–20 μm observations can better constrain the photometry. If the IRAS fluxes are confirmed, then a warm-grain component needs to be added to the model, such as from a circumstellar disk or nonequilibrium small-grain heating.

4.3. HD 23362

Assuming a K2V spectral type, Sylvester et al. (1996) determine that the photometric distance to HD 23362 is 6.5 pc. This contrasts sharply against the subsequent *Hipparcos* parallax measurement that places HD 23362 at 352 pc. The derived visual extinction of ~ 2 mag (Table 3) is also inconsistent with the Sylvester et al. (1996) distance. In view of the high reddening, Sylvester et al. (1996) comment that the distance to HD 23362 should be determined independently and that the star may be misclassified.

In order to produce a closer match to the *Hipparcos* distance, we re-calculate the extinction values assuming the spectral type is K2III, with $T_{eff}=4200$ and $R=20R_{\odot}$ (Tables 3 and 4). With this assumption we are then able to fit the optical and NIR photometric data with a stellar blackbody at 187 pc (Table 5, Fig. 6). The model dust cloud parameters are similar to those of HD 4881, except that there is no disagreement between the model SED and the 12 μm IRAS flux (Fig. 6).

Sylvester & Skinner (1996) attempted to fit the SED with a model circumstellar disk, but failed to fit the 100 μm flux by an order of magnitude. They concluded that the 100 μm is due to infrared cirrus. Our model suggests that the 12 μm – 25 μm emission is photospheric, and that all of the 60 μm – 100 μm emission is attributable to interstellar dust. Model 23362-b (Table 5, Fig. 6) indicates that R_{out} may be as small as 1.1×10^4 AU and still fit the IRAS PSC 100 μm data. In this case the cloud subtends $\sim 1'$ radius and would be unresolved in the IRAS 60–100 μm data.

4.4. HD 23680

As with HD 23362, the photometric distance for HD 23680 given the G5V spectral type is ~ 20 pc (Sylvester & Skinner 1996), but both the *Hipparcos* parallax and the reddening are consistent with $d \sim 200$ pc. We recalculate the reddening values assuming HD 23680 has spectral type G5III, and using $T_{eff}=5050$ and $R=10R_{\odot}$, we fit the stellar SED using distance $d=205$ pc (Table 5, Fig. 7). The cloud model (23680-a) gives satisfactory fits with $R_{out} = 7 \times 10^4$ AU, which subtends $\sim 6'$ radius. However, the second model (23680-b), with $R_{out} = 4 \times 10^4$ AU, also gives an SED passing within the error bars of the $100 \mu\text{m}$ data point. In this case, the cloud's $\sim 3'$ radius may be resolved in the $100 \mu\text{m}$ IRAS data. In our optical data, resolved patches of nebulosity are detected as far as $1.7'$ from the star, particularly to the north-northeast, with surface brightness $R = 24 \text{ mag arcsec}^{-2}$. Inspection of the IRAS Sky Survey Atlas at $100 \mu\text{m}$ shows an asymmetric morphology extended $\sim 3'$ north of the stellar position. Thus, the smaller outer radius for model 23680-b is preferred over model 23680-a. As with HD 23362, Sylvester & Skinner (1996) could not fit the IRAS data with a circumstellar disk model. In particular, the circumstellar disk model could not reproduce the $100 \mu\text{m}$ flux. Rather, the simple cloud model demonstrated here is consistent with the FIR data.

4.5. HD 26676 & HD 49662

For both of these B stars the dust cloud model cannot fit the $12-25 \mu\text{m}$ and $60-100 \mu\text{m}$ regions simultaneously, as was found for the Pleiads 18 Tau and 21 Tau. In Table 5 and Figs. 8 and 9 we show two different models for fitting the $12-25 \mu\text{m}$ data separately from the $60-100 \mu\text{m}$ data. The models fitting the $12-25 \mu\text{m}$ emission require inner boundaries extending closer to the stars, and with greater dust number densities, than the dust cloud models that fit the $60-100 \mu\text{m}$ data. A number density distribution increasing toward the star, such as with a circumstellar disk, could also enhance the $12 \mu\text{m}$ and $25 \mu\text{m}$ fluxes. Thus it is possible that these stars have circumstellar disks and happen to be interacting with ISM. Alternately, the excess $12-25 \mu\text{m}$ emission could originate from non-equilibrium small-grain heating. As discussed in Section 3, HD 26676 is physically associated with the Pleiades. Castelaz et al. (1987) demonstrated that nonequilibrium grain heating in the Pleiades nebulosity produces $\sim 30\%$ of the total $12-100 \mu\text{m}$ emission at $12 \mu\text{m}$ and $25 \mu\text{m}$. Models 26676-a and 49662-a in Figs. 8 and 9 generate only $\sim 10\%$ of the total observed emission at $12-25 \mu\text{m}$. Thus, an added small-grain component could alter the resulting SED to fit the data. If this is true, then evidence should also exist for NIR excess or infrared emission features (Sellgren et al. 1996). We have no NIR data for HD 26676, but the NIR data for HD 49662 is consistent with a purely photospheric origin. The scale of emission for models HD 26676-a and HD 49662-a, given the distances listed in Table 5, is $\sim 5.5'$, which is consistent with the $\sim 10'$ radii measured by Gaustad & Van Buren (1993) in IRAS Skyflux plates.

4.6. HD 123160

The photometric distance of 16 pc assuming that HD 123160 is a G5V star (Sylvester et al. 1996) is inconsistent with the lack of parallax information from the *Hipparcos* and *Gliese* catalogs, and with the high extinction (Table 3). Though we confirm that the optical and NIR data may be fit with a G5V star at 16 pc, a nearly equal model SED is obtained by assuming a G0III star at \sim 110 pc. For either spectral type the visual extinction exceeds 2 magnitudes (Table 3). In Fig. 10 and Table 5 we present dust cloud models assuming HD 123160 is a distant giant. However, further study of this system is necessary to determine its evolutionary status. Lithium abundance measurements suggest that HD 123160 is relatively young, with age \sim 70 Myr (Dunkin, Barlow, & Ryan 1997). This age is comparable to that of many Vega-like stars as well as members of the Pleiades. The nebulosities *iia* and *iib* (Fig. 2) may originate from the same physical mechanisms that produce the IC 349 nebulosity near 23 Tau in the Pleiades (Herbig 1996; Herbig & Simon 2001). The semi-stellar appearance of *iia* is similar to the main knot in IC 349 (Herbig 1996; Herbig & Simon 2001), except that it is very red (Section 3). On the other hand, the entire complex of nebulous features shown in Fig. 1F resembles a star-forming region where a young star illuminates its natal dust cloud. Feature *iia* could be a K star associated with HD 123160. The SED's produced by our Pleiades cloud model fit the observed 12–100 μ m data points (Fig. 10), and the scale of emission for the models is \sim 1.5' radius. This corresponds to the projected separation between HD 123160 and feature *iv* (Fig. 4F). A circumstellar disk model used by Sylvester & Skinner (1996), assuming HD 123160 is a G5V star at 16 pc, also gives satisfactory fits to the data. However, the present high resolution data (Fig. 2) show no evidence for a circumstellar disk, and we therefore favor the Pleiades cloud model.

5. Discussion

Backman & Paresce (1993) cautioned that thermal emission from reflection nebulosities such as in the Pleiades may appear similar to thermal emission from Vega-like stars. Our simulations of interstellar grain emission demonstrate that the nebulae shown in Fig. 1 are capable of producing the excess thermal emission observed by IRAS. In three cases, a circumstellar disk or non-equilibrium small-grain heating may account for the 12–25 μ m emission. The latter mechanism is consistent with our current understanding of grain emission from the Pleiades.

A general problem in interpreting SEDs is that the models typically have as many adjustable parameters as there are data points. Good fits are not persuasive by themselves to determine the distribution of the dust, especially when the dust is optically thin to absorption and emission. Unlike the SEDs of young stellar objects, the Vega-like stars have strongly peaked far-infrared flux densities consistent with dust with a small range of temperatures. To interpret the dust distributions as lying in a single plane (disks) requires additional information, such as images of the scattered light.

Other authors have fitted the IRAS data for HD 4881, HD 23362, HD 23680, and HD 123160 with circumstellar disk models, and in some cases interpreted excess emission at 100 μm as due to infrared cirrus (Low et al. 1984) in the background. Given the optical data and the results of our modeling, we argue that the infrared cirrus is local to each star, appearing as the Pleiades Phenomenon in scattered light. From the infrared standpoint, the term “cirrus hotspot” is used to describe the local heating of ISM by a star. To qualify as cirrus hotspots, FIR emission must be extended on arcminute scales with color temperatures between 25 K and 70 K (Gaustad & Van Buren 1993). The early-type stars in the Pleiades, for example, appear as cirrus hotspots in the IRAS data. The three B stars in our list, HD 4881, HD 26676, and HD 49662, are also identified as infrared cirrus hotspots (Gaustad & Van Buren 1993; Dring et al. 1996).

Our three B stars, as well as 18 Tau and 21 Tau from the original sample, are given as Vega excess stars by Backman & Paresce (1993) in their Table VIII. We find that all but three of the remaining 29 B stars in the Backman & Paresce (1993) table are also identified as cirrus hotspots by Gaustad & Van Buren (1993). The two different interpretations for the same FIR data illustrate the difficulty in uniquely identifying the origin of dust that produces excess thermal emission. For instance, Backman & Paresce (1993) identified Vega-like stars if the color temperature satisfied $30 \text{ K} < T < 500 \text{ K}$, which overlaps the color temperature criterion adopted by Gaustad & Van Buren (1993). However, the Vega-like stars with resolved debris disks and rings (e.g. β Pic, ϵ Eri, Fomalhaut, HR 4796A) have heliocentric distances $d < 100 \text{ pc}$, whereas the stars discussed here are located at $d > 100 \text{ pc}$. Thus the unique identification of thermal excess is problematic for the more distant objects. From our initial sample of 79 Vega-like stars, 72 have *Hipparcos*-detected distances, and of these 43 (60%) have $d > 100 \text{ pc}$. In part, the source confusion is a question of spatial resolution. Resolved observations from the optical to the far-infrared are essential for determining the nature of circumstellar dust. However, the Sun also lies within a relatively ISM-free bubble 65–250 pc in radius (Sfeir et al. 1999). Thus, the Pleiades phenomenon naturally occurs with greater frequency among the more distant stars.

Though distance is a first order measure for the reliability of identifying the Vega Phenomenon, the Local Bubble has a non-spherical geometry, giving specific directions with respect to the Sun that are most likely to contain denser ISM that would produce the Pleiades Phenomenon. Sfeir et al. (1999) use the NaI D-line doublet to measure absorption toward stars within 300 pc of the Sun, and produce maps of neutral gas in three galactic projections. In Figs. 11, 12, and 13, we plot the locations of Vega-like stars using the same same galactic projections as Sfeir et al. (1999). We take the 60 Vega-like stars from Backman & Paresce (1993) Table VIII (“Bright star catalog main-sequence stars with Vega-like far-infrared excesses”), and 73 Vega-like stars from Mannings & Barlow (1998) Table 2 (“Newly identified candidate main-sequence stars with debris disks”). Two stars (HD 73390 and HD 181296) in Mannings & Barlow (1998) are in the Backman & Paresce (1993) table, leaving a total sample of 131 stars. From this sample we select the 111 stars that have *Hipparcos*-detected distances. Finally, a total of 85 Vega-like stars lie within the three planes of reference defined by Sfeir et al. (1999), and those within 300 pc of the Sun are plotted in Figs.

11–13. We overlay two contours that trace the lowest and highest NaI D2 absorption mapped by Sfeir et al. (1999). The figure captions give more details.

Figures 11–13 show that the walls of the Local Bubble approach the Sun <50 pc in certain directions, but are >100 pc distant in other directions, particularly toward the North Galactic Pole (Fig. 13; named the “Local Chimney” by Welsh et al. 1999). In the galactic plane view (Fig. 11) the Local Bubble has maximum extend toward $l=225^\circ$, which is also the direction toward HD 49662. However, HD 49662 is located right on the wall of the high density gas. Three more Vega-like stars in Fig. 11 (HD 52140, HD 28149 and HD 108257) appear spatially associated with local overdensities of gas.

Figure 12 shows that HD 23680 is in the same general direction of HD 26676 and both are within the region of high-density gas. Also evident is a group of five stars that trace the high-density wall at $l=180^\circ$, $b \sim -30^\circ$, $d \sim 125$ pc. These Vega-like stars (HD 23324 = 18 Tau, HD 23432 = 21 Tau, HD 28149, HD 28375, HD 28978) are associated with Taurus and the Pleiades. Two more groups of five stars each appear in Fig. 12. At $l=0^\circ$, $b \sim -30^\circ$, $d \sim 50$ pc we find HD 181296, HD 191089, HD 176638, HD 181864, and HD 181327. These are not associated with gas, but HD 181296 and HD 181327 are members of the Tucanae Association (Zuckerman & Webb 2000). Their youth and the lack of interstellar gas favors the Vega Phenomenon interpretation of their FIR excesses. A third group of Vega-like stars is evident at $l=0^\circ$, $b \sim 25^\circ$, $100 \text{ pc} < d < 150 \text{ pc}$ (HD 142096, HD 142165, HD 143018, HD 145263, and HD 145482). These are at the distance and direction of the Upper Scorpius subgroup of the Sco OB2 association (de Zeeuw et al. 1999) which is encompassed by a giant reflection nebula (Gordon et al. 1994). The association of these stars with large-scale dust and gas favors the Pleiades Phenomenon interpretation for the FIR excesses.

Figure 13 shows that Vega-like stars may be detected at the greatest distances with the least confusion from the ISM in the direction of the North Galactic Pole. The figure also shows a group of four stars at $l=90^\circ$, $b \sim -30^\circ$, $d \sim 20$ pc (HD 39060 = β Pic, HD 41742, HD 53143, and HD 67199). Their location in the Local Bubble and their association with β Pic favors the Vega Phenomenon explanation for their FIR excesses.

Overall, the fraction of Vega-like stars that lie at or beyond the Local Bubble wall (thin contour) is $>50\%$. In Fig. 11 we plot 40 Vega-like stars, but only five are in the Local Bubble. The remainder are located at or beyond the wall of low density gas, and 16 of these are in high density gas regions. Another 11 stars from the Backman & Paresce (1993) and Mannings & Barlow (1998) tables would appear in Fig. 11 if we plotted distances between 300 and 600 pc. From the 30 Vega-like stars plotted in Fig. 12, 16 are in the high-density gas and 6 more lie between the high density and low density walls. In Fig. 13, 6 Vega-like stars are in the Local Bubble, 4 lie between the low and high density walls, and 4 more are found in the high density regions.

The post-*Hipparcos* distance determinations are not only useful for judging the position of Vega-like stars relative to the Local Bubble, they also help evaluate the physical scale of thermal emission. We found that the *Hipparcos* parallaxes for HD 23362, HD 23680, and HD 123160, as

well as the large reddening values, probably place these stars beyond 100 pc, rather than 6–16 pc, as determined in pre-*Hipparcos* investigations. The greater distances therefore explain how the thermal emission may originate from ISM material extending 10^3 – 10^5 AU from each star and still meet the criteria for inclusion in the IRAS PSC. The possibility that these stars are distant giants producing the Pleiades Phenomenon may help explain the infrared excesses observed around ~ 100 luminosity class III stars (Zuckerman et al. 1995; Jura 1999; Kim et al. 2001).

6. Summary

We detect optical reflection nebulosity around six main-sequence stars that are candidates for having debris disks. Five nebulae share the morphological characteristics of dust surrounding bright stars in the Pleiades. The environment of HD 123160 has features that resemble both the Pleiades and star forming regions. No disk-like structures are detected, though our optical coronagraphic technique does not probe the circumstellar environment closer than $\sim 4''$ radius. The sensitivity-limited radii of the nebulosities are between $1'$ and $2'$ and the radial measurements of surface brightness are consistent with uniform density dust clouds illuminated by the central star.

We show that thermal emission from an optically thin, uniform density dust cloud surrounding HD 23362, HD 23680, and HD 123160 can entirely explain the 12–100 μm emission detected by IRAS. The Pleiades Phenomenon, a random encounter between a clump of ISM and a star, is the most likely explanation for the excess FIR emission. For HD 4881, HD 26676, and HD 49662, the blackbody cloud model cannot simultaneously fit the 12–25 μm and 60–100 μm regions of the IRAS-detected SED. These stars may have circumstellar disks in addition to the interstellar dust detected in the optical. However, the excess 12–25 μm emission may also arise from non-equilibrium heating of small grains. We show that 18 Tau and 21 Tau in the Pleiades have comparable SED's with signatures of hot grains in the 12–25 μm fluxes. Future observations sensitive to disk-like structure within 500 AU of each star, and that search for NIR excesses and emission features, are necessary to determine if these stars are manifesting the Vega Phenomenon and the Pleiades Phenomenon simultaneously.

We find that most Vega-like B stars have also been associated with FIR cirrus hotspots. We demonstrate that >50% of Vega Phenomenon stars are located beyond the gas-poor Local Bubble, and many are spatially associated with regions of high density neutral gas. Thus, a significant fraction of Vega Phenomenon stars beyond 100 pc may be confused with Pleiades Phenomenon stars.

Acknowledgements: We are grateful to J. Gradie, B. Zuckerman, and E. Becklin for access to their coronagraph. This work was supported in part by NASA grants to DCJ and PK, and by the NSF Center for Adaptive Optics, managed by UC Santa Cruz under cooperative agreement AST-9876783. This research has made use of the NASA/IPAC Infrared Science Archive, operated by JPL, California Institute of Technology.

REFERENCES

Arny, T. 1977, *ApJ*, 217, 83

Artymowicz, P. & Clampin, M. 1997, *ApJ*, 490, 863

Aumann, H.H. 1988, *AJ*, 96, 1415

Aumann, H.H. 1985, *PASP*, 97, 885

Aumann, H.H., Gillett, F.C., Beichman, C.A., et al. 1984, *ApJ*, 278, L23

Backman, D. E. & Paresce, F. 1993, in *Protostars and Planets III*, eds. E. H. Levy & J. I. Lunine, (Univ. Arizona Press, Tucson), p. 1253

Backman, D. E. & Gillett, F. C. 1987, in *Cool Stars, Stellar Systems, and the Sun*, ed. J. L. Linsky & R. E. Stencel, (Springer: Berlin), p. 340

Castelaz, M.W., Sellgren, K. & Werner, M.W. 1987, *ApJ*, 313, 853

Cox, A. 1999, *Allen's Astrophysical Quantities*, (AIP Press: New York).

Coulson, I.M., Dent, D.M. & Dent, W.R.F. 1998, *MNRAS*, 296, 934

Desert, F.-X., Boulanger, F. & Puget, J.L. 1990, *A&A*, 237, 215

Dring, A.R., Murthy, J., Henry, R.C. & Walker, H.J. 1996, *ApJ*, 457, 764

Dunkin, S.K., Barlow, M.J., & Ryan, S.G. 1997, *MNRAS*, 290, 165

Gaustad, J.E. & Van Buren, D. 1993, *PASP*, 105, 1127

Gordon, K.D., Witt, A.N., Carruthers, G.R., Christensen, S.A. & Dohne, B.C. 1994, *ApJ*, 432, 641

Greenberg, J.M. 1968, in *Nebulae & Interstellar Matter*, eds. B.M. Middlehurst and L.H. Aller, (Univ. Chicago Press: Chicago), p. 221

Herbig, G.H. 1996, *AJ*, 111, 1241

Herbig, G.H. & Simon, T. 2001, *AJ*, 121, 3138.

Jura, M. 1999, *ApJ*, 515, 706

Kalas, P. 1998, *Earth, Moon and Planets*, 81, 27

Kalas, P. & Jewitt, D. 1996, *AJ*, 111, 1347

Kim, S.S., Zuckerman, B. & Silverstone, M. 2001, *ApJ*, 550, 1000

Lagrange, A.-M., Backman, D.E. & Artymowicz, P. 2000, in *Protostars and Planets IV*, eds. V. Mannings, A.P. Boss & S.S. Russell, (Univ. Arizona Press: Tucson), p. 1253

Lloyd, J.P., Liu, M.C., Macintosh, B.A., et al. 2000, SPIE Proceedings, 4008, pg. 814.

Low, F.J. et al. 1984, ApJ, 278, L19

Mannings, V. & Barlow, M.J. 1998, ApJ, 497, 330

Mathis, J.S. 1990, ARA&A, 28, 37

Max, C.E., Olivier, S.S., Friedman, H.W., et al. 1997, *Science*, 277, 1649

Meyer, M.R., Calvet, N. & Hillenbrand, L.A. 1997, AJ, 114, 288

Miroshnichenko, A.S., Mulliss, C.L., Bjorkman, K.S., et al. 1999, MNRAS, 302, 612

Nakajima, T. & Golimowski, D.A. 1995, AJ, 109, 1181

Plets, P. 1999, A&A, 343, 496

Racine, R. 1968, AJ, 73, 233

Sellgren, K., Werner, M.W., & Allamandola, L.J. 1996, ApJS, 102, 369

Sellgren, K., Luan, L. & Werner, M.W. 1990, ApJ, 359, 384

Sellgren, K. 1984, ApJ, 277, 623

Sfeir, D.M., Lallement, R., Crifo, F. & Welsh, B.Y. 1999, A&A, 346, 785

Sylvester, R.J., Skinner, C.J., Barlow, M.J. & Mannings, V. 1996, MNRAS, 279, 915

Sylvester, R.J. & Skinner, C.J. 1996, MNRAS, 283, 457

Sylvester, R.J., Skinner, C.J. & Barlow, M.J. 1997, MNRAS, 289, 831

van den Bergh, S. 1966, AJ, 71, 990

Welsh, B.Y., Sfeir, D.M., Sirk, M.M. & Lallement, R. 1999, A&A, 352, 308

White, R.E. & Bally, J. 1993, ApJ, 409, 234

de Zeeuw, P.T., Hoogerwerf, R., de Bruijne, J.H.J., Brown, A.G.A. & Blaauw, A. 1999, AJ, 117, 354

Zuckerman, B. & Webb, R.A. 2000, ApJ, 535, 959

Zuckerman, B., Kim, S.S. & Liu, T. 1995, ApJ, 446, L79

Table 1: Summary of Observations

| Name | Date (UT) | Telescope | λ (μm) | R_{in}^* (arcsec) | Integration (sec) | SpT | Parallax (mas) | Nebulosity |
|-----------|-----------|------------|-----------------------------|---------------------|-------------------|-------|--------------------|------------|
| HD 4881 | 10/12/93 | UH 2.2 m | 0.65 | 4.0 | 640 | B9.5V | 2.84 | Pleiades |
| HD 23362 | 01/30/00 | ... | 0.65 | 4.5 | 285 | K2V | 3.24 | Pleiades |
| HD 23680 | 01/30/00 | ... | 0.65 | 4.5 | 600 | G5V | 5.54 | Pleiades |
| HD 26676 | 10/12/93 | ... | 0.65 | 4.0 | 320 | B8Vn | 6.49 | Pleiades |
| HD 49662 | 01/30/00 | ... | 0.65 | 6.7 | 640 | B7IV | 5.37 | Pleiades |
| HD 123160 | 01/29/00 | ... | 0.65 | 4.1 | 510 | G5V | -0.01 [†] | Double Arm |
| ... | 01/30/00 | ... | 0.55 | 3.7 | 120 | ... | ... | ... |
| ... | 06/17/00 | Lick 3.0 m | 2.15 | 2.5 | 360 | ... | ... | ... |
| ... | 06/03/01 | ... | 2.15 | 4.0 | 720 | ... | ... | ... |
| ... | 06/03/01 | ... | 1.66 | 4.0 | 600 | ... | ... | ... |

*Radius from target star blocked by coronagraphic occulting spot and PSF residuals.

[†]Negative value in *Hipparcos Catalog* indicates parallax measurement that is smaller than the error. In section 4.6 we estimate $d \sim 110$ pc.

Table 2: Optical through Far-Infrared Fluxes (not dereddened or color-corrected)*

| $\lambda(\mu\text{m}) =$ | 0.44 (mag) | 0.55 (mag) | 0.88 (mag) | 1.22 (mag) | 1.65 (mag) | 2.18 (mag) | 3.55 (mag) | 4.77 (mag) | 12 (Jy) | 25 (Jy) | 60 (Jy) | 100 (Jy) |
|--------------------------|---------------|---------------|---------------|---------------|---------------|---------------|---------------|---------------|------------|------------|------------|-------------|
| HD 4881 | - | - | - | - | - | - | - | - | 0.28 | 0.28 | 3.88 | 11.2 |
| | 6.25 | 6.22 | 6.17 | 5.99 | 5.99 | 5.96 | - | - | 0.36 | 0.39 | 4.75 | 11.5 |
| HD 23362 | 9.53 | 7.85 | 6.07 | - | - | - | 3.72 | 3.98 | 1.42 | 0.50 | 0.67 | 2.88 |
| | 9.62 | 7.91 | 6.18 | 4.89 | 4.05 | 3.85 | - | - | 1.38 | 0.44 | 0.72 | 6.32 |
| HD 23680 | 9.40 | 8.60 | - | 6.01 | 5.37 | 5.24 | 5.16 | 5.29 | 0.44 | - | 1.89 | 6.27 |
| | 9.62 | 8.39 | 7.20 | - | - | - | - | - | 0.43 | 0.19 | 2.08 | 6.02 |
| HD 26676 | - | - | - | - | - | - | - | - | 1.15 | 6.43 | 26.3 | 37.2 |
| | 6.26 | 6.24 | 6.20 | - | - | - | - | - | 1.49 | 7.41 | 30.0 | 47.4 |
| HD 49662 | 5.30 | 5.40 | - | 5.7 | 5.5 | 5.6 | 5.8 | - | 0.43 | 1.62 | 4.60 | 5.68 |
| | 5.29 | 5.39 | 5.47 | - | 5.61 | 5.59 | - | - | - | - | - | - |
| HD 123160 | 10.12 | 8.62 | 6.94 | 5.86 | 5.07 | 4.87 | 4.73 | 5.33 | 0.60 | 0.38 | 3.03 | 3.97 |
| | 10.25 | 8.66 | 7.05 | - | - | - | - | - | 0.62 | 0.37 | 3.11 | 4.41 |
| 18 Tau | - | - | - | - | - | - | - | - | 0.47 | 0.59 | 2.99 | 6.01 |
| | 5.60 | 5.66 | 5.69 | - | - | - | - | - | 0.42 | 0.74 | 3.52 | 12.80 |
| 21 Tau | - | - | - | - | - | - | - | - | 0.42 | 1.14 | 4.68 | 10.90 |
| | 5.72 | 5.76 | 5.74 | - | - | - | - | - | 0.39 | 1.06 | 13.20 | 9.75 |

*0.44 – 0.88 μm from Sylvester et al. (1996) (first row) and *Hipparcos* (second row), 1.22 – 2.18 μm from Sylvester et al. (1996) (first row) and 2MASS (second row), 3.55 – 4.77 μm from Sylvester et al. (1996), 12 – 100 μm fluxes from IRAS PSC (first row) and IRAS FSC (second row)

Table 3: Extinction assuming $A_V = 3.0E(B - V)$ and $A_V = 1.1E(V - K)^*$

| Name | SpT | $B - V$ | $(B - V)_o$ | $E(B - V)$ | $V - K$ | $(V - K)_o$ | $E(V - K)$ | A_V | A_V |
|-----------|-------|---------|-------------|------------|---------|-------------|------------|-----------|-----------|
| | | | Obs. | | | Obs. | | $(B - V)$ | $(V - K)$ |
| HD 4881 | B9.5V | 0.03 | -0.07 | 0.10 | 0.26 | -0.13 | 0.39 | 0.30 | 0.43 |
| | B8V | ... | -0.11 | 0.14 | ... | -0.24 | 0.50 | 0.42 | 0.55 |
| HD 23362 | K2V | 1.70 | 0.91 | 0.79 | 4.03 | 2.22 | 1.81 | 2.37 | 1.99 |
| | K2III | ... | 1.16 | 0.54 | ... | 2.70 | 1.33 | 1.62 | 1.46 |
| HD 23680 | G5V | 1.01 | 0.68 | 0.33 | 3.26 | 1.59 | 1.67 | 0.99 | 1.84 |
| | G5III | ... | 0.86 | 0.15 | ... | 2.10 | 1.16 | 0.45 | 1.28 |
| HD 26676 | B8Vn | 0.02 | -0.11 | 0.13 | - | - | - | 0.39 | - |
| HD 49662 | B7IV | -0.10 | -0.14 | 0.04 | -0.20 | -0.29 | 0.09 | 0.12 | 0.10 |
| HD 123160 | G5V | 1.55 | 0.68 | 0.87 | 3.77 | 1.59 | 2.18 | 2.61 | 2.40 |
| | G0III | ... | - | - | ... | 1.75 | 2.02 | - | 2.22 |
| 18 Tau | B8V | -0.06 | -0.11 | 0.05 | - | - | - | 0.15 | - |
| 21 Tau | B8V | -0.04 | -0.11 | 0.07 | - | - | - | 0.21 | - |

*The observed magnitudes used here are the average of the two values given for each passband in Table 2.

A_V from $V - K$ was used to determine A_λ for Table 4 except when $V - K$ data not available.

Table 4: De-reddened optical and NIR magnitudes and color-corrected FIR fluxes*

| $\lambda(\mu\text{m}) =$ | 0.44 (mag) | 0.55 (mag) | 0.88 (mag) | 1.22 (mag) | 1.65 (mag) | 2.18 (mag) | 3.55 (mag) | 4.77 (mag) | 12 (Jy) | 25 (Jy) | 60 (Jy) | 100 (Jy) |
|--------------------------|---------------|---------------|---------------|---------------|---------------|---------------|---------------|---------------|------------|------------|------------|-------------|
| HD 4881 (B9.5V) | - | - | - | - | - | - | - | - | 0.19 | 0.20 | 2.94 | 10.28 |
| | 5.69 | 5.79 | 5.97 | 5.87 | 5.92 | 5.91 | - | - | 0.25 | 0.27 | 3.60 | 10.55 |
| (B8V) | - | - | - | - | - | - | - | - | - | - | - | - |
| | 5.54 | 5.67 | 5.91 | 5.84 | 5.90 | 5.90 | - | - | - | - | - | - |
| HD 23362 (K2V) | 6.90 | 5.86 | 5.12 | - | - | - | 3.63 | 3.93 | 1.00 | 0.36 | 0.51 | 2.64 |
| | 6.99 | 6.45 | 5.23 | 4.33 | 3.70 | 3.64 | - | - | 0.97 | 0.31 | 0.54 | 5.80 |
| (K2III) | 7.60 | 6.39 | 5.37 | - | - | - | 3.65 | 3.94 | - | - | - | - |
| | 7.69 | 6.45 | 5.48 | 4.48 | 3.79 | 3.69 | - | - | - | - | - | - |
| HD 23680 (G5V) | 6.96 | 6.76 | - | 5.49 | 5.05 | 5.04 | 5.07 | 5.24 | 0.31 | - | 1.43 | 5.75 |
| | 7.18 | 6.55 | 6.32 | - | - | - | - | - | 0.30 | 0.13 | 1.58 | 5.52 |
| (G5III) | 7.71 | 7.32 | - | 5.65 | 5.15 | 5.10 | 5.10 | 5.26 | - | - | - | - |
| | 7.93 | 7.11 | 6.59 | - | - | - | - | - | - | - | - | - |
| HD 26676 (B8Vn) | - | - | - | - | - | - | - | - | 0.79 | 4.56 | 19.92 | 34.13 |
| | 5.74 | 5.85 | 6.01 | - | - | - | - | - | 1.03 | 5.26 | 22.73 | 43.49 |
| HD 49662 (B7IV) | 5.16 | 5.30 | - | 5.67 | 5.48 | 5.59 | 5.79 | - | 0.30 | 1.15 | 3.48 | 5.21 |
| | 5.15 | 5.29 | 5.42 | - | 5.59 | 5.58 | - | - | - | - | - | - |
| HD 123160 (G5V) | 6.92 | 6.22 | 5.78 | 5.18 | 4.68 | 4.61 | 4.61 | 5.27 | 0.42 | 0.27 | 2.30 | 3.64 |
| | 7.05 | 6.26 | 5.89 | - | - | - | - | - | 0.43 | 0.26 | 2.36 | 4.04 |
| (G5III) | 7.16 | 6.40 | 5.87 | 5.23 | 4.68 | 4.63 | 4.62 | 5.27 | - | - | - | - |
| | 7.29 | 6.44 | 5.98 | - | - | - | - | - | - | - | - | - |
| 18 Tau (B8V) | - | - | - | - | - | - | - | - | 0.33 | 0.42 | 2.27 | 5.51 |
| | 5.40 | 5.51 | 5.62 | - | - | - | - | - | 0.29 | 0.53 | 2.67 | 11.74 |
| 21 Tau (B8V) | - | - | - | - | - | - | - | - | 0.29 | 0.81 | 3.55 | 10.00 |
| | 5.62 | 5.55 | 5.64 | - | - | - | - | - | 0.27 | 0.75 | 10.00 | 8.94 |

*Table rows have same format as Table 2, except that a second spectral type is given for several stars. The change in the FIR color correction for the second spectral type is negligible and not listed.

Table 5: Pleiades Model: Uniform density dust cloud

| Star - Model | T_{eff} (K) | d (pc) | $R_\star (\times 10^{11})$ (cm) | $\rho (\times 10^{-23})$ (g cm $^{-3}$) | r_{in} (AU) | R_{out} (AU) | T_o (K) | τ_{max} | L_d/L_\star |
|--------------|------------------|-----------|------------------------------------|---|------------------|-------------------|--------------|----------------------|----------------------|
| HD 4881-a | 12,300 | 168 | 2.09 | 0.27 | 800 | 10^5 | 146 | 1.6×10^{-3} | 1.9×10^{-3} |
| -b | ... | ... | ... | 0.29 | 300 | 8.7×10^4 | 217 | 1.5×10^{-3} | 1.8×10^{-3} |
| HD 23362-a | 4200 | 187 | 13.92 | 0.37 | 400 | 2.0×10^5 | 148 | 4.5×10^{-3} | 2.0×10^{-3} |
| -b | ... | ... | ... | 0.38 | 40 | 1.1×10^4 | 366 | 2.6×10^{-3} | 1.2×10^{-3} |
| HD 23680-a | 5050 | 205 | 6.97 | 2.30 | 200 | 7.0×10^4 | 176 | 9.8×10^{-3} | 4.7×10^{-3} |
| -b | ... | ... | ... | 3.20 | 400 | 4.0×10^4 | 134 | 7.7×10^{-3} | 4.3×10^{-3} |
| HD 26676-a | 11,600 | 163 | 2.09 | 2.50 | 100 | 5.5×10^4 | 320 | 8.4×10^{-3} | 1.0×10^{-2} |
| -b | ... | ... | ... | 22.0 | 50 | 3.0×10^3 | 421 | 4.0×10^{-3} | 4.4×10^{-2} |
| HD 49662-a | 14,000 | 180 | 2.47 | 0.13 | 100 | 6.2×10^4 | 397 | 4.9×10^{-4} | 5.9×10^{-4} |
| -b | ... | ... | ... | 0.70 | 10 | 1.1×10^4 | 1000 | 4.8×10^{-4} | 5.7×10^{-4} |
| HD 123160-a | 5,500 | 110 | 4.18 | 4.9 | 300 | 1.2×10^4 | 135 | 3.5×10^{-3} | 2.1×10^{-3} |
| -b | ... | 120 | ... | ... | 200 | 1.1×10^4 | 158 | 3.2×10^{-3} | 2.0×10^{-3} |
| 18 Tau-a | 11,400 | 125 | 2.00 | 0.21 | 200 | 6.0×10^4 | 236 | 7.7×10^{-4} | 2.2×10^{-5} |
| -b | ... | ... | ... | 0.18 | 200 | 1.6×10^5 | 236 | 1.8×10^{-3} | 1.9×10^{-5} |
| 21 Tau-a | 11,400 | 125 | 2.00 | 0.32 | 10 | 6.0×10^4 | 770 | 1.2×10^{-3} | 4.3×10^{-5} |
| -b | ... | ... | ... | 1.0 | 10 | 2.8×10^4 | 770 | 1.7×10^{-3} | 1.3×10^{-4} |

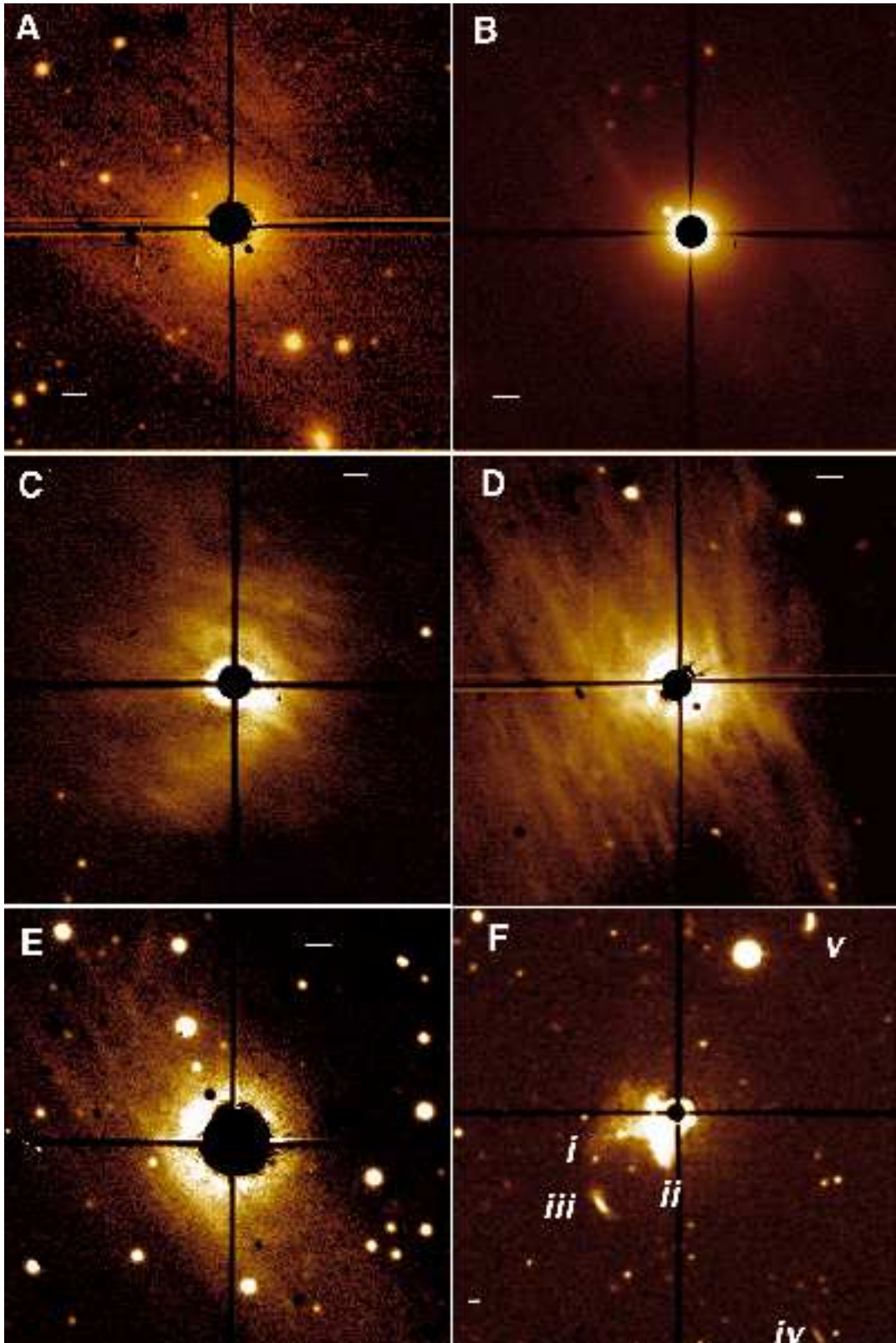


Fig. 1.— R-band coronagraphic images of six Vega-like stars after PSF subtraction [A: HD 4881, B: HD 23362 C: HD 23680, D: HD 26676, E: HD 49662, F: HD 123160]. North is up, east is left, the white bar represents 5'', and each box is 1.5' on a side, except for F which is 3.0' on a side. For F we label five regions of nebulosity discussed in the text. Negative features are artifacts of the PSF subtraction step.

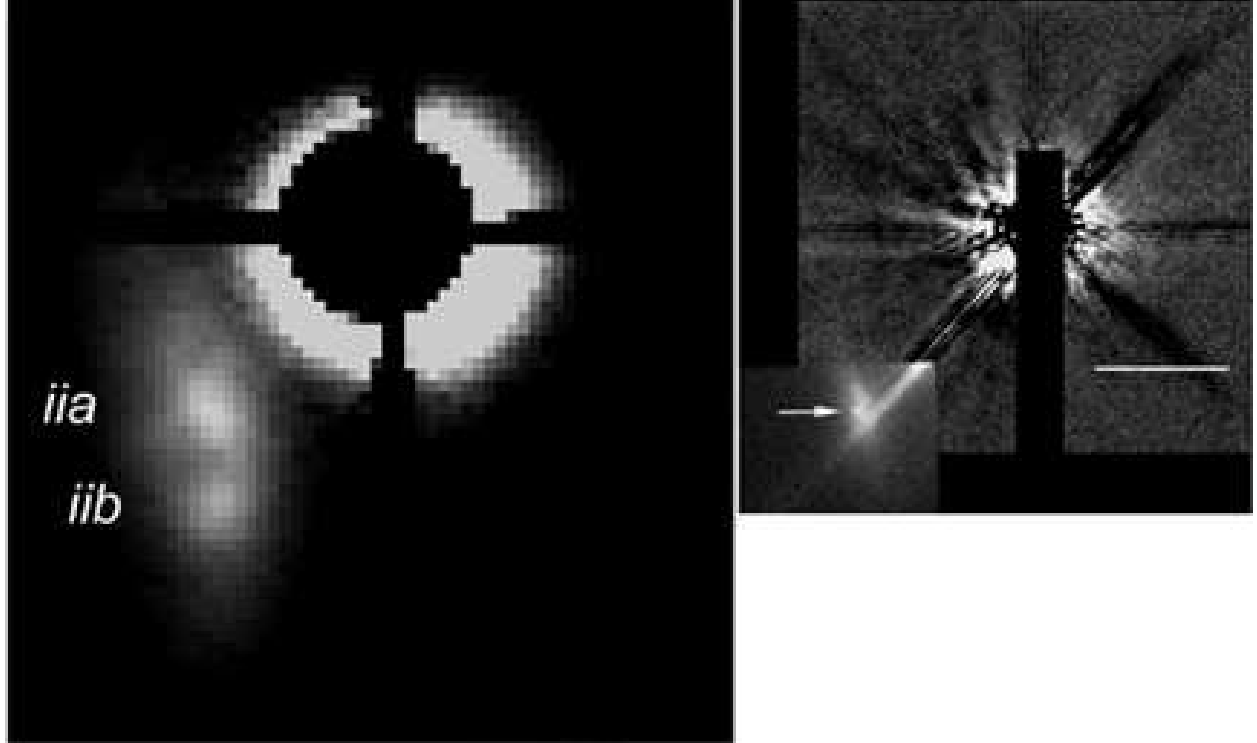


Fig. 2.— The left panel is a different grayscale stretch and field of view of Fig. 1F, showing the existence of 2 brightness peaks within arm *ii*. The right panel shows the same field imaged with adaptive optics at $2.15 \mu\text{m}$ on two different nights. The wide field shows the 17 June 2000 data where HD 123160 was placed behind the occulting finger and a PSF template was subtracted to search for disk-like nebulosity. In the lower left of this frame we superimpose the 03 June 2001 *K*-band data which has higher signal-to-noise due to the greater integration time (Table 1) and the fact that no PSF template is subtracted. In both *K*-band data sets, as well as the *H*-band data, feature *iia* is detected as a possible point source at $\text{PA} \sim 135^\circ$, indicated here with an arrow. The white bar represents $5''$.

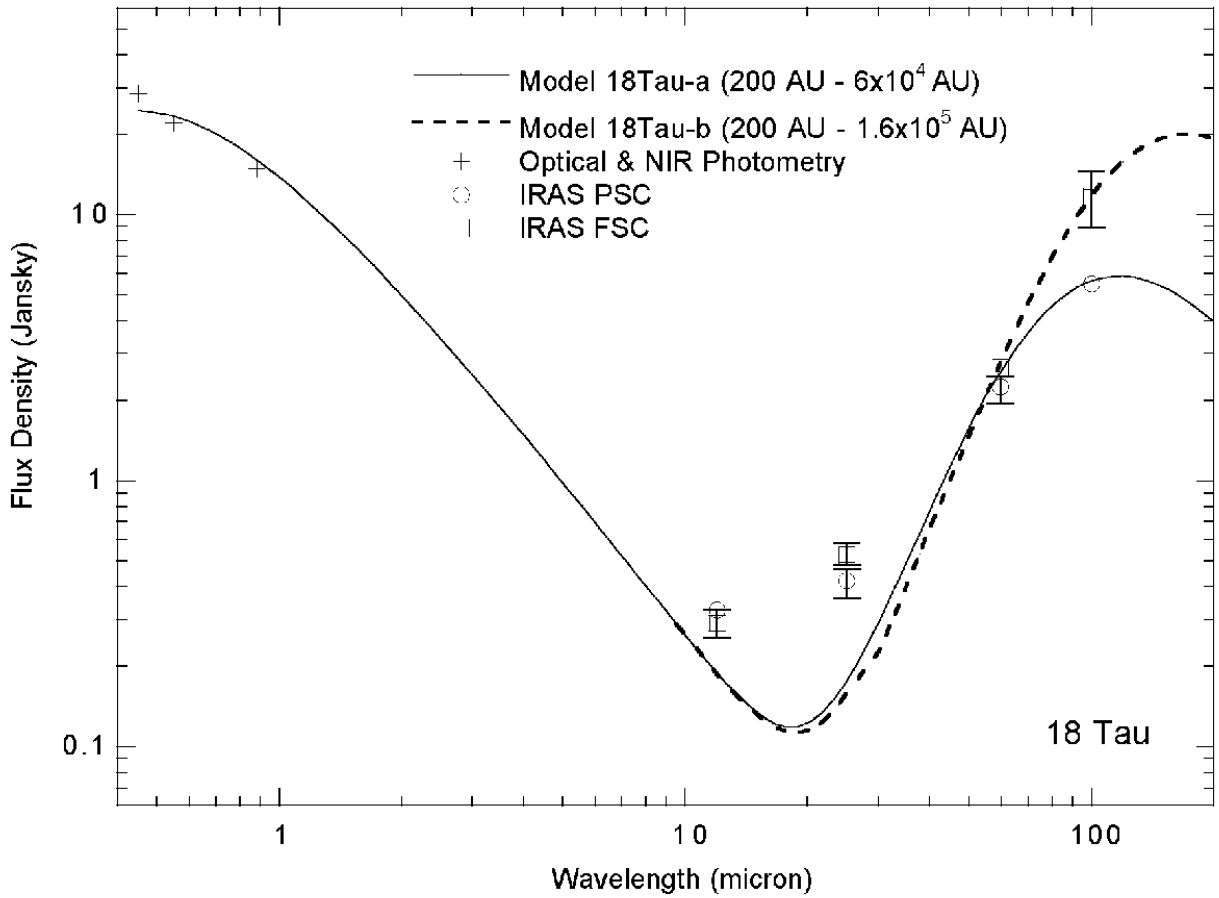


Fig. 3.— Photometric data for 18 Tau (Table 4) and spectral energy distributions from dust cloud models (Table 5). Symbol sizes for the IRAS data approximate the sizes of error bars unless marked otherwise. The two models demonstrate different cloud properties that give fits to either the PSC or FSC 100 μ m data. However, the model cannot fit the 12-25 μ m and 60-100 μ m regions simultaneously, confirming previous findings (Castelaz et al. 1987). Non-equilibrium heating of small grains is thought to produce flux in excess of the 12-25 μ m blackbody emission simulated here.

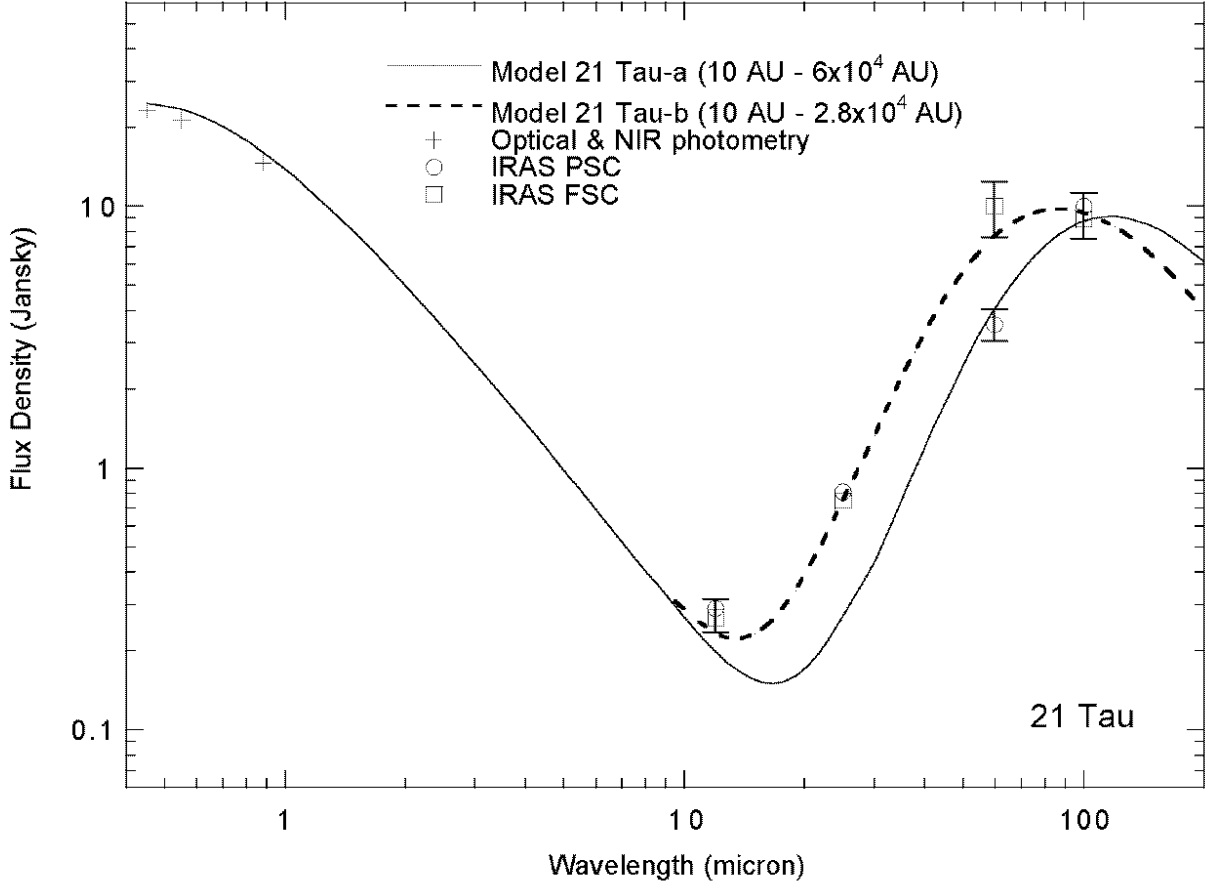


Fig. 4.— Photometric data for 21 Tau (Table 4) and spectral energy distributions from dust cloud models (Table 5). Symbol sizes for the IRAS data approximate the sizes of error bars unless marked otherwise. The two models demonstrate different cloud properties that give fits to either the PSC or FSC 100 μ m data. For the IRAS PSC data, the observed SED is similar to that of 18 Tau (Fig. 3). Model 21 Tau-a has $r_{in}=10$ AU, but the hotter dust relative to the 18 Tau models (Fig. 3) does not produce enough 12-25 μ m flux to fit the observations. A key difference in the IRAS FSC data for 21 Tau is the greater 60 μ m flux density. This permits a fit to the entire SED with Model 21 Tau-b (Table 5).

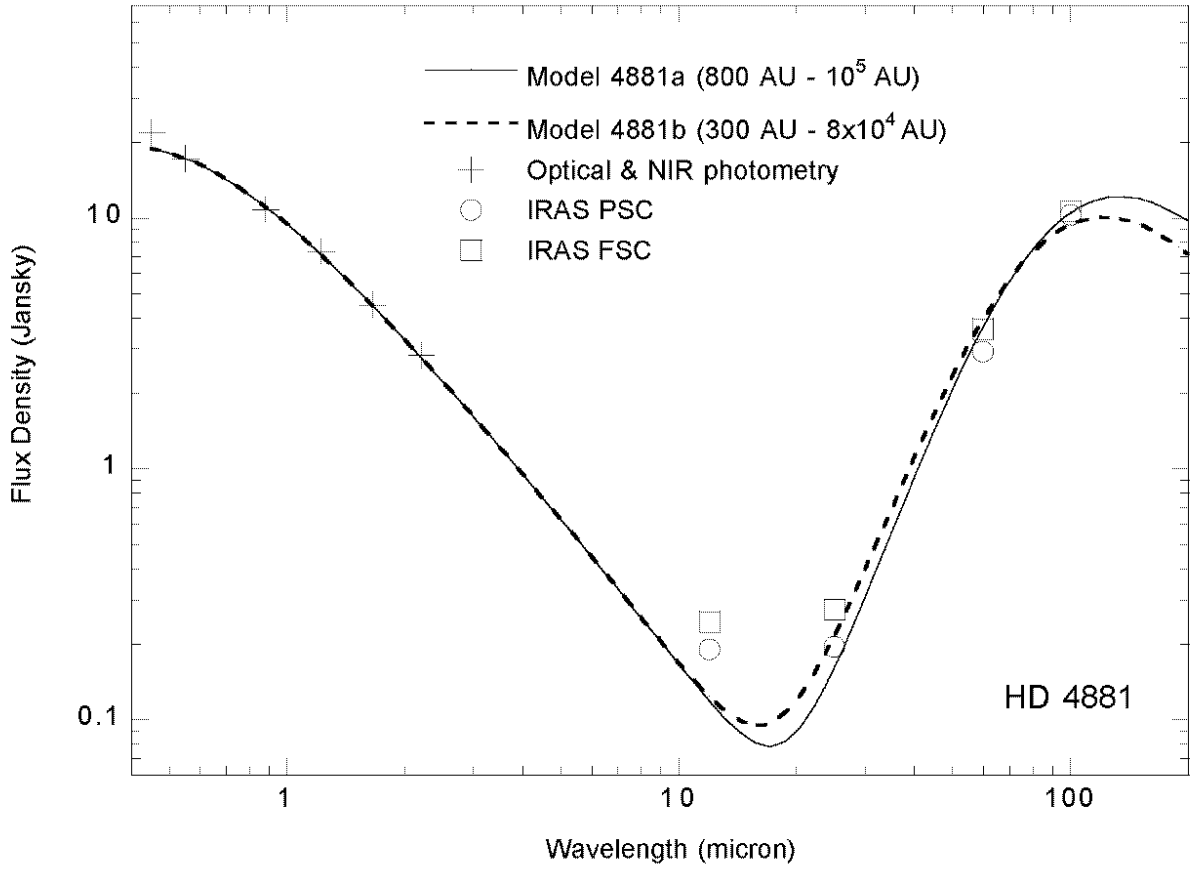


Fig. 5.— Photometric data for HD 4881 (Table 4) and spectral energy distributions from two dust cloud models (Table 5). Symbol sizes for the IRAS data approximate the sizes of error bars. The two models demonstrate different cloud dimensions that give SED's consistent with the 25–100 μm data. Model 4881-b demonstrates that decreasing outer radius relative to model 4881a diminishes the 100 μm emission. Decreasing the inner radius in Model 4881-b enhances the 25 μm emission, but with negligible effect on the 12 μm emission. The 12 μm emission should be mostly photospheric, but the IRAS data do not lie on the extrapolated photospheric blackbody curve.

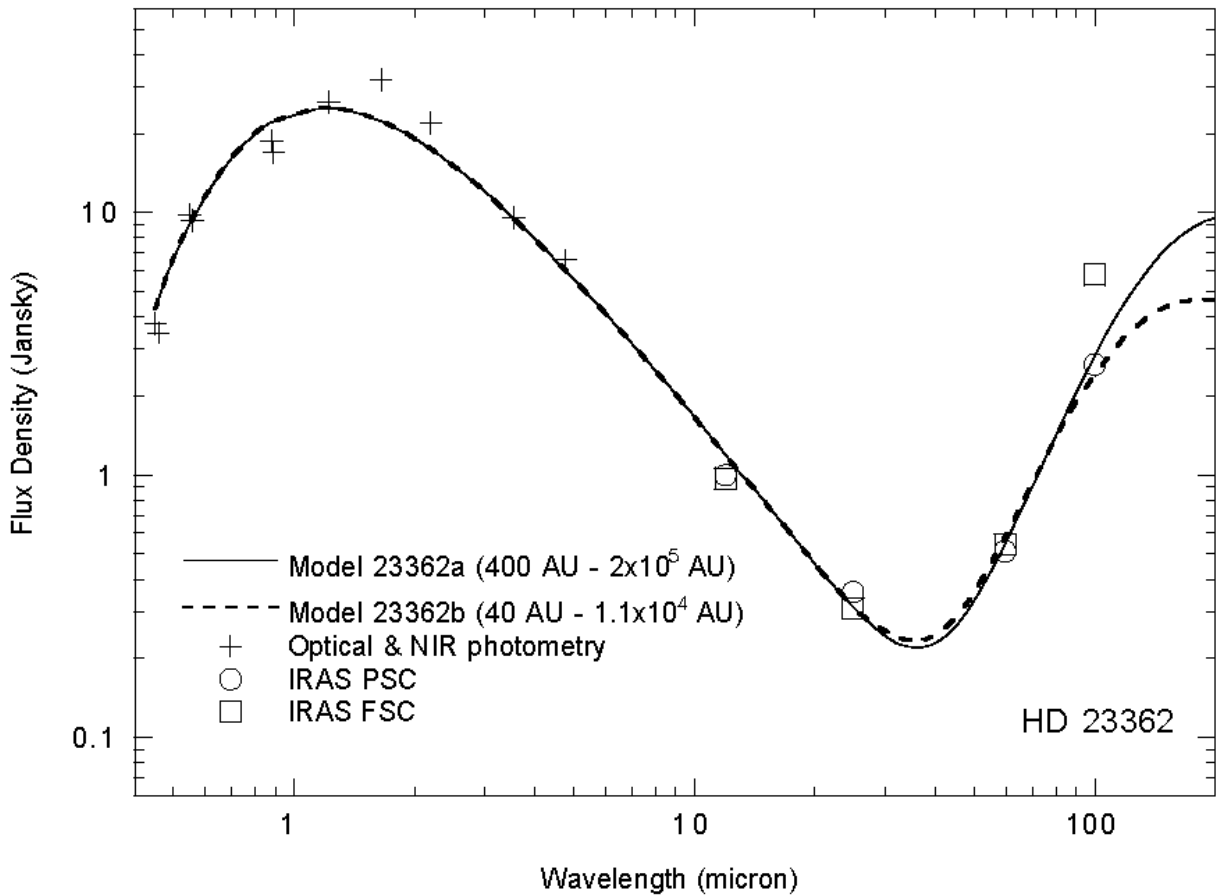


Fig. 6.— Photometric data for HD 23362 (Table 4) and spectral energy distributions from two dust cloud models (Table 5). Symbol sizes for the IRAS data approximate the sizes of error bars. The two models demonstrate different cloud dimensions that fit the entire 12-100 μ m PSC SED.

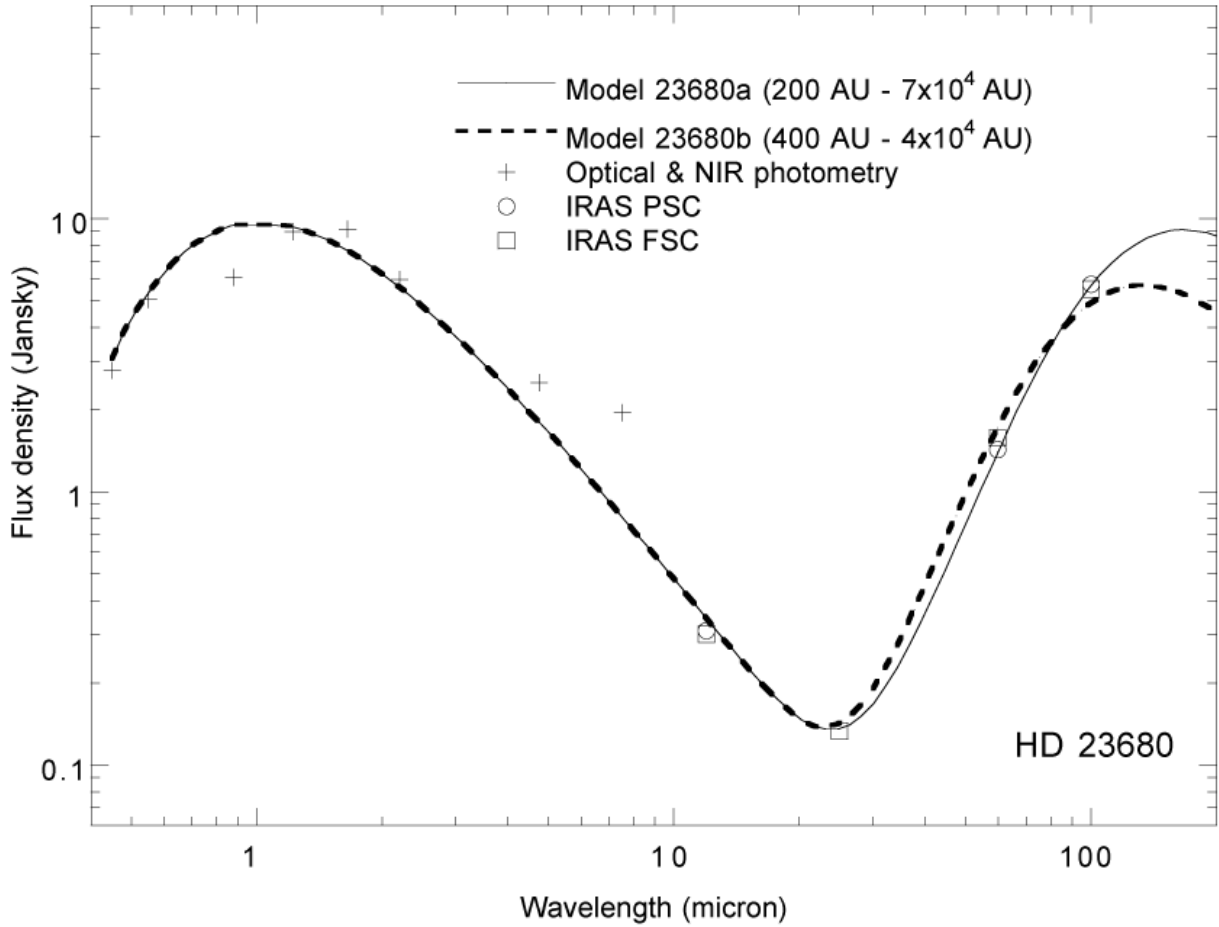


Fig. 7.— Photometric data for HD 23680 (Table 4) and spectral energy distributions from two dust cloud models (Table 5). Symbol sizes for the IRAS data approximate the sizes of error bars unless marked otherwise. The two models demonstrate different cloud dimensions that fit the entire 12-100 μ m SED.

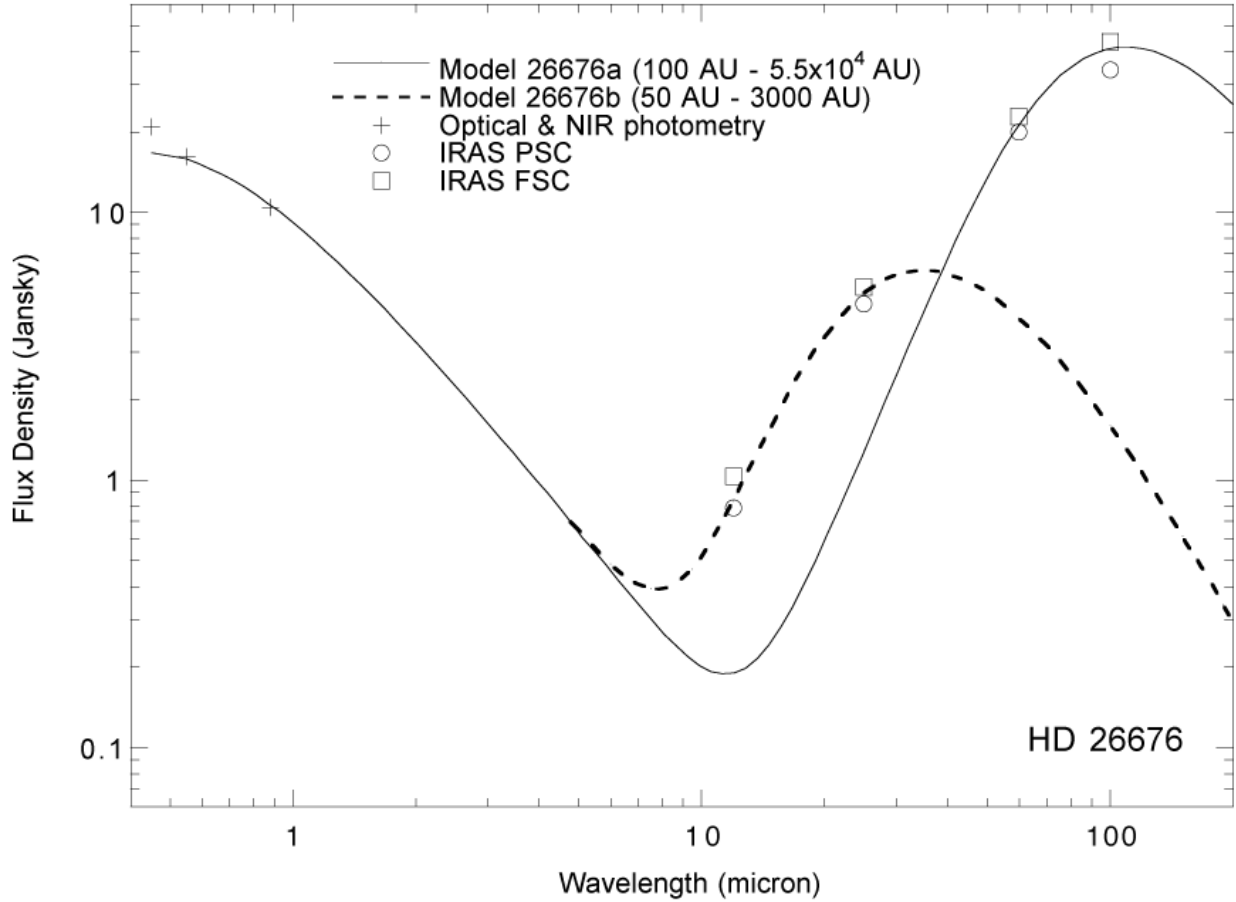


Fig. 8.— Photometric data for HD 26676 (Table 4) and spectral energy distributions from two dust cloud models (Table 5). Symbol sizes for the IRAS data approximate the sizes of error bars. As with the Pleiads 18 Tau and 21 Tau (Figs. 3 and 4), no single model can simultaneously fit the 12-25 μ m and 60-100 μ m regions of the SED simultaneously. These two regions are fit independently by models 26676-a and 26676-b.

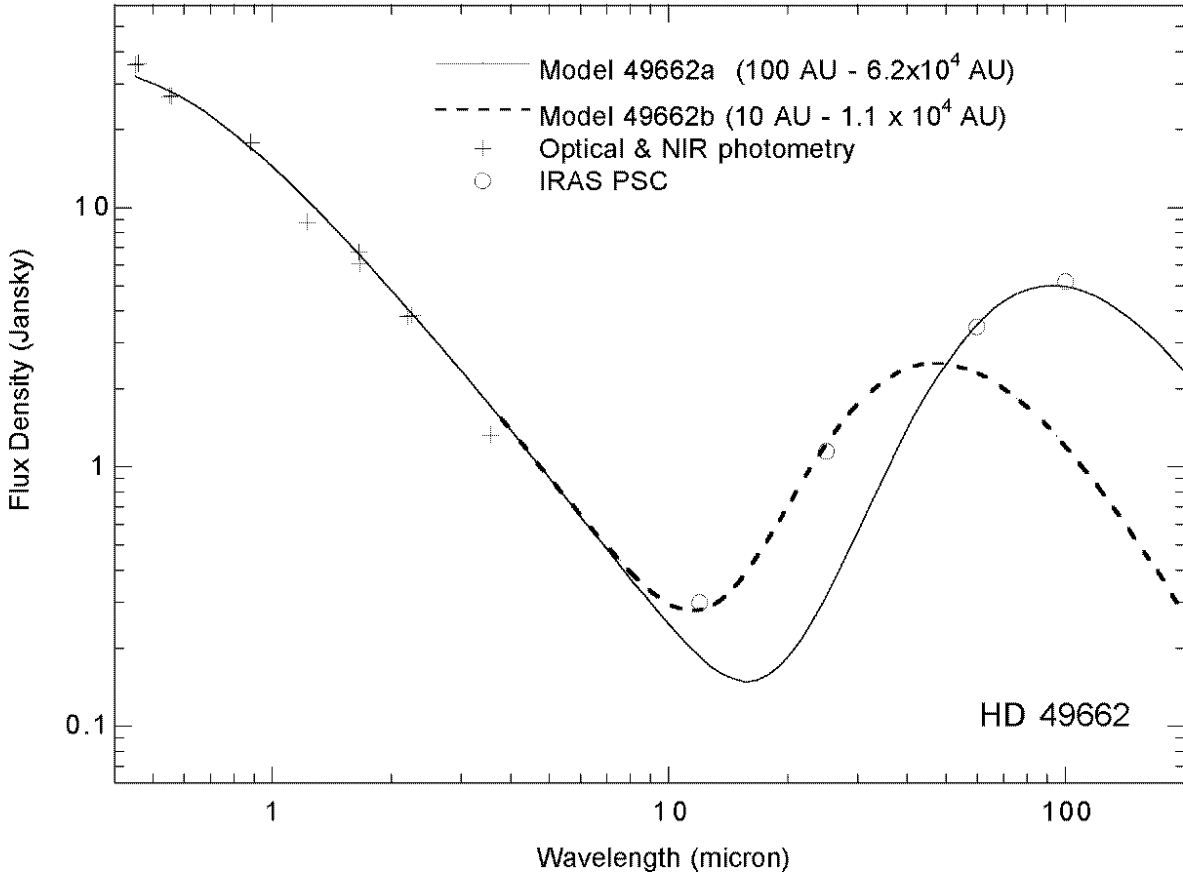


Fig. 9.— Photometric data for HD 49662 (Table 4) and spectral energy distributions from dust cloud models (Table 5). Symbol sizes for the IRAS data approximate the sizes of error bars. As with 18 Tau, 21 Tau, and HD 26676 (Figs. 3, 4 and 8), no single model can simultaneously fit the 12-25 μm and 60-100 μm regions of the SED simultaneously. These two regions are fit independently by models 49662-a and 49662-b (Table 5).

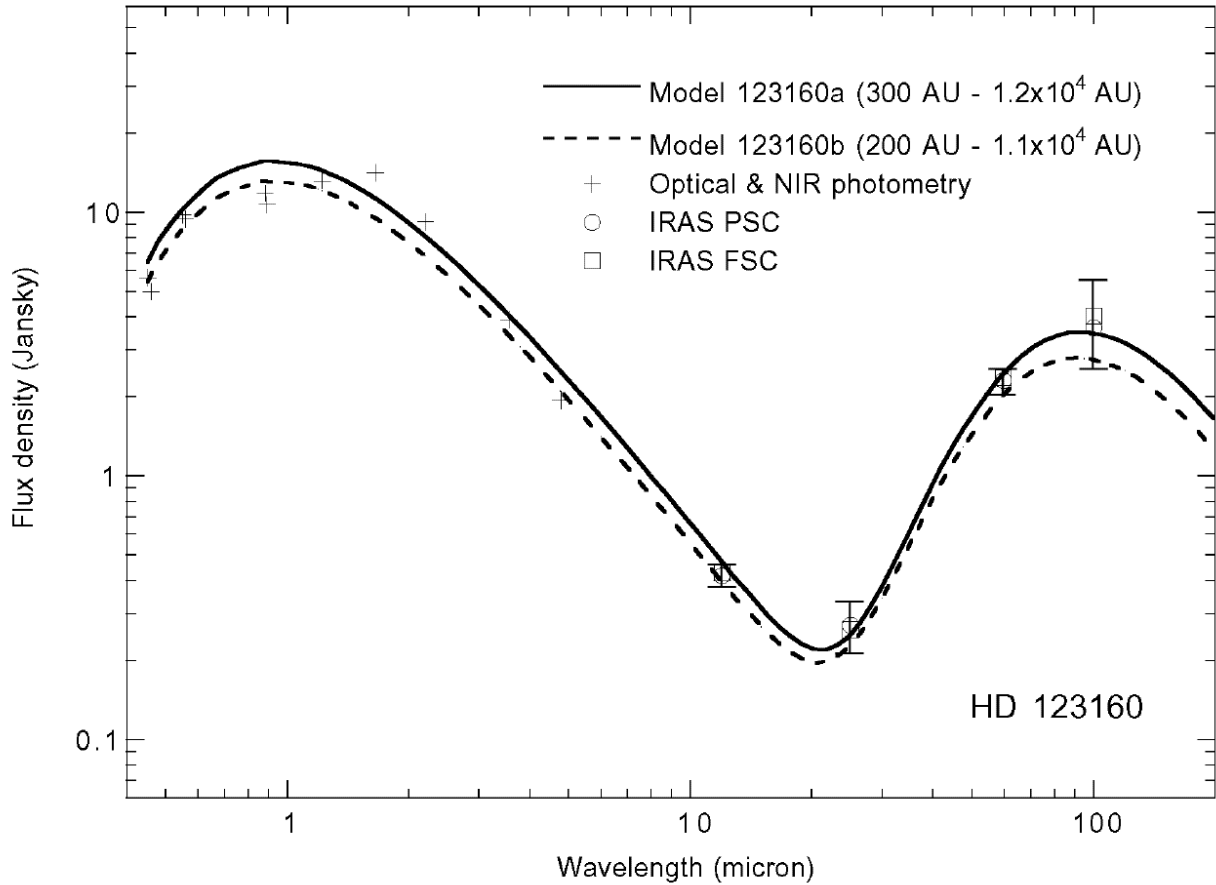


Fig. 10.— Photometric data for HD 123160 (Table 4) and spectral energy distributions from dust cloud models (Table 5). Symbol sizes for the IRAS data approximate the sizes of error bars unless marked otherwise. The two models demonstrate different cloud radii that fit the data. With model 123160-b, we demonstrate that the distance could be increased to $d=120$ pc and still obtain a satisfactory fit to the SED between $0.45 \mu\text{m}$ and $12 \mu\text{m}$.

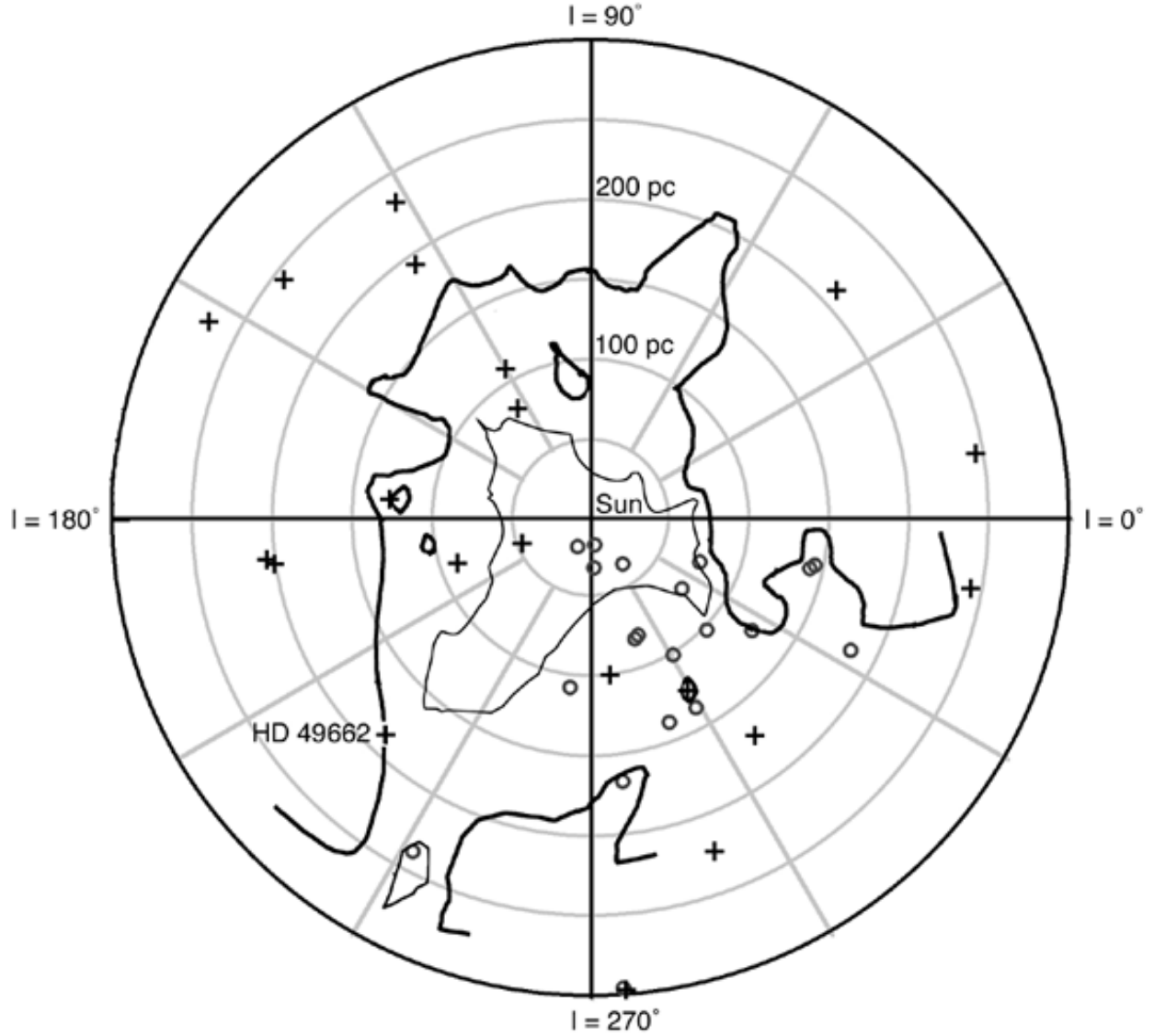


Fig. 11.— Galactic plane (downward) view of Vega-like stars from Backman & Paresce 1993 (crosses) and Mannings & Barlow 1998 (circles). The Sun is at the center. Following Sfeir et al. (1999), only stars that have $-18^\circ < b < 18^\circ$ are plotted, and the Sun–star distance is the *Hipparcos* distance irrespective of the angle above or below the reference plane. The isocontours trace the NaI gas absorption from Fig. 3 in Sfeir et al. (1999). The thin and thick contours correspond to the $5 \text{ m}\text{\AA}$ and $>50 \text{ m}\text{\AA}$ D2-line equivalent widths, respectively. One exception is the closed contour near $l=240^\circ$, $d = 250 \text{ pc}$ which traces a $20 \text{ m}\text{\AA}$ equivalent width isocontour from Sfeir et al. (1999). We show it because the Vega-like source HD 52140 falls within the contour boundary. Two more examples of Vega-like stars associated with a local overdensities of gas are HD 28149 at $l=174^\circ$, $d = 127 \text{ pc}$ and HD 108257 at $l=299^\circ$, $d = 123 \text{ pc}$.

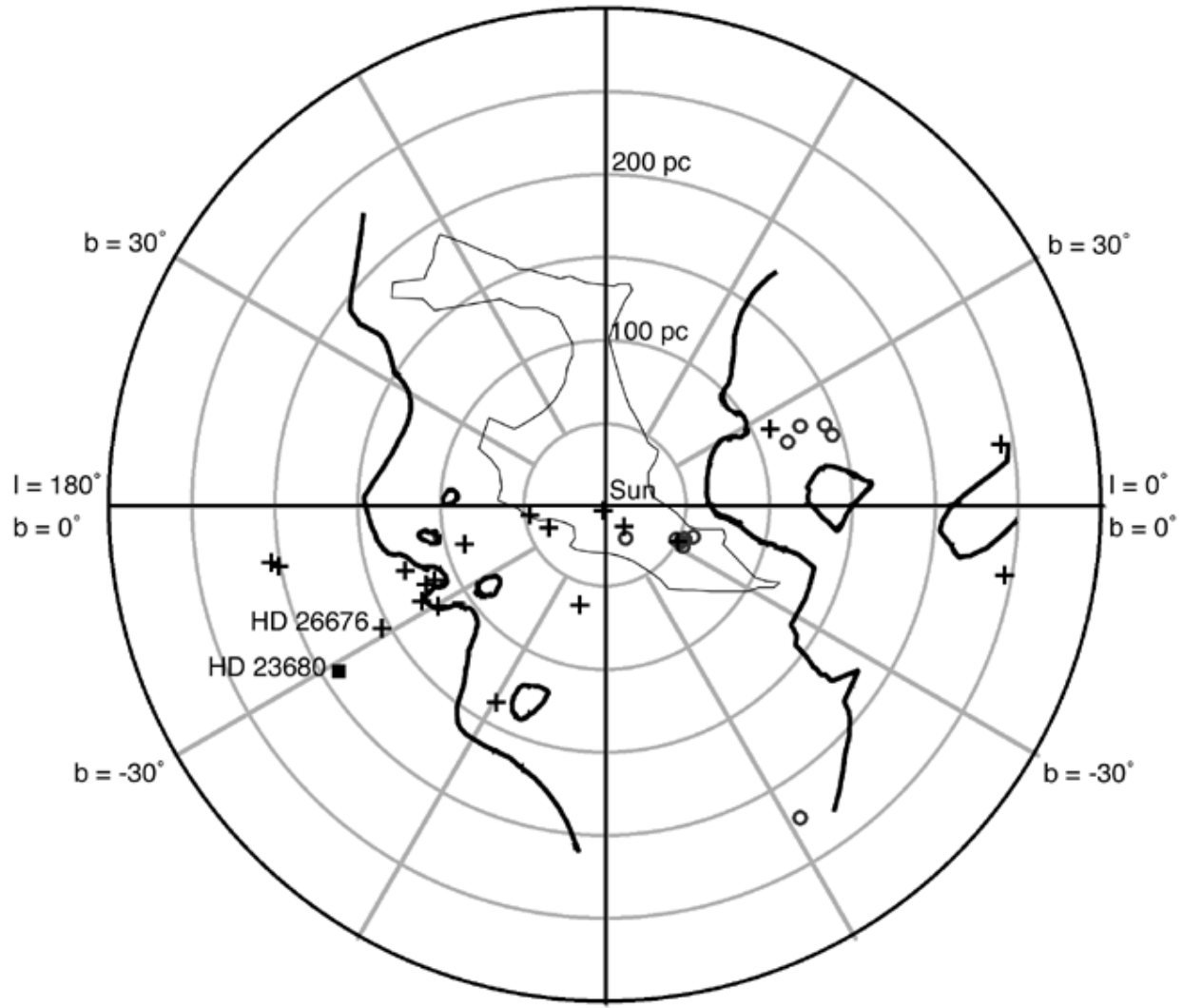


Fig. 12.— Meridian plane view, perpendicular to the galactic plane, and containing both galactic poles and the galactic center to the right. Symbols and contours same as Fig. 11. Stars plotted if they fall within $l=0^\circ \pm 18^\circ$ or $l=180^\circ \pm 18^\circ$. HD 23680 from our study falls within these limits and is plotted with a solid square.

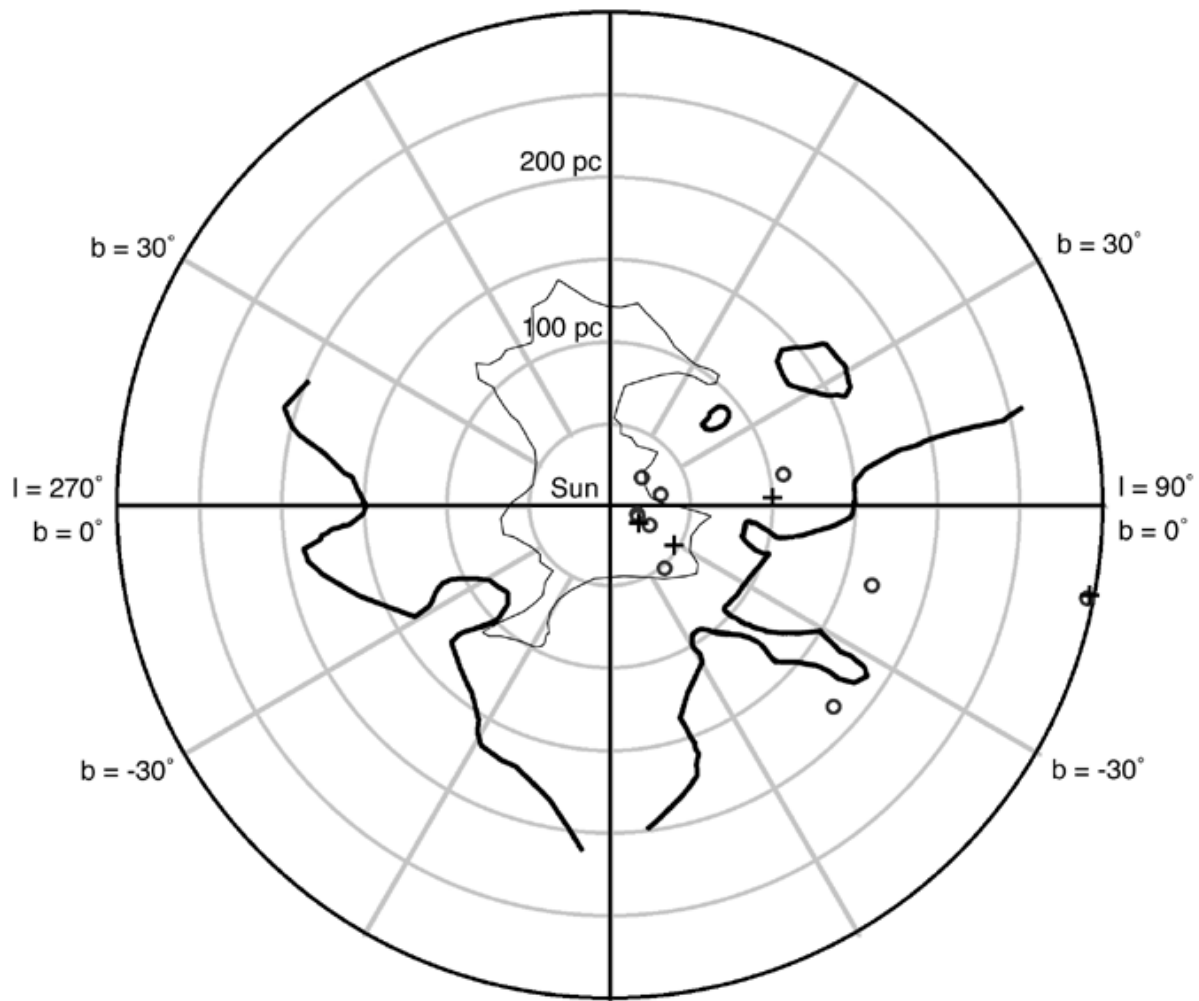


Fig. 13.— Galactic rotation plane, perpendicular to both the galactic plane and to the galactic center direction. Symbols and contours same as Fig. 11. Star plotted if they fall within $l=90^\circ \pm 18^\circ$ or $l=270^\circ \pm 18^\circ$.